# Synergistic impact of corrosion pitting on the rotating bending fatigue of additively manufactured 316L stainless steel: Integrated experimental and modeling analyses

International Journal of Fatigue 188 (2024) 108491

Contents lists available at ScienceDirect

International Journal of Fatigue

journal homepage: www.elsevier.com/locate/ijfatigue

# Synergistic impact of corrosion pitting on the rotating bending fatigue of additively manufactured 316L stainless steel: Integrated experimental and modeling analyses

Alireza Behvar [a,1], Yahya Aghayar [b,1], Maryam Avateffazeli [a], Andrea Tridello [c], Alessandro Benelli [c], Davide S. Paolino [c], Mohsen Mohammadi [b], Meysam Haghshenas [a,*]

[a] Fatigue, Fracture, and Failure Laboratory (F3L), Department of Mechanical, Industrial, and Manufacturing Engineering, University of Toledo, OH 43606, USA
[b] Marine Additive Manufacturing Centre of Excellence (MAMCE), University of New Brunswick, Fredericton, NB E3B5A3, Canada
[c] Dipartimento di Ingegneria Meccanica e Aerospaziale, Politecnico di Torino, Corso Duca Degli Abruzzi 24, 10129 Torino, Italy

ARTICLE INFO

*Keywords:*
Additive manufacturing
Rotating bending fatigue
Corrosion-fatigue
Laser powder bed fusion
Stainless steel 316L

ABSTRACT

In this study, the ex-situ rotating bending corrosion fatigue behavior of laser powder bed fused stainless steel (SS) 316L has been studied incorporating experimental analyses and modeling. The findings revealed significant variations (almost 20 %) in fatigue lifetime in pre-corroded specimens relative to non-corroded (virgin) specimens because of corrosion-derived pitting phenomena on the surface. To this end, the fatigue strength of virgin (non-corroded) and pre-corroded SS 316L were recorded at 242 MPa and 203 MPa, respectively. Upon conducting the fatigue tests and extracting stress-life trends, advanced microstructural characterization and post-mortem analyses were used to quantify fatigue crack behavior and fracture surface. An empirical model is also developed employing depth-sensing indentation testing, linear elastic fracture mechanics, and computer tomography scans to propose an optimum predictive trend. The analysis comparing existing models with our proposed model demonstrates reasonable agreement between experimental findings and the predicted life for the studied laser powder bed fused SS 316L material exposed to corrosion rotating bending fatigue test. The findings of this research carry important contributions to the structural integrity and longevity of marine engineering, ship construction, naval operations, and naval aviation where materials and components are exposed to cyclic loading and corrosion.

## 1. Introduction

Given the necessity for alloys to function in challenging service conditions under cyclic loadings, the investigation of fatigue in harsh conditions has emerged as a prominent area of research in contemporary times. The fatigue performance of the metal in corrosive environments exhibits a decreased strength compared to its performance in ambient-air conditions. Considering that corrosion and fatigue phenomena are both influenced by surface quality [1,2], particularly in metals produced through additive manufacturing (AM) processes, it is necessary to employ specialized equipment to comprehensively examine the impact of these events on the durability properties of materials, taking into account the significant role played by the surface. To this end, rotating bending fatigue (RBF) testing is a reliable choice, as it can apply a gradient of peak stress on the surface, hence facilitating the examination

*Abbreviations:* AM, Additive Manufacturing; AM'd, Additively Manufactured; ANOVA, Analysis of Variance; ASTM, American Society for Testing and Materials; CDF, Cumulative Distribution Function; CLS, Crystallographic Line Segment; CM'd, Conventionally Manufactured; CNC, Computer Numerical Control; $CuSO_4$, Cupric sulphate; EBSD, Electron Backscatter Diffraction; EDM, Electrical Discharge Machining; EDS, Energy Dispersive Spectroscopy; EVD, Extreme Value Distribution; GB, Grain Boundary; HCF, High Cycle Fatigue; HCl, Hydrochloric acid; IAMA, Internal Average Misorientation Angle; ISO, International Organization for Standardization; KAM, Kernel Average Misorientation; LAGB, Low Angle Grain Boundary; LCF, Low Cycle Fatigue; LEFM, Linear Elastic Fracture Mechanic; LPBF, Laser Powder Bed Fusion; MLE, Maximum Likelihood Estimation; OM, Optical Microscopy; PDF, Probability Density Function; pH, Potential of Hydrogen; PSB, Persistent Slip Band; RBF, Rotating Bending Fatigue; RBCF, Rotating Bending Corrosion Fatigue; SEM, Scanning Electron Microscopy; SIF, Stress Intensity Factor; SS, Stainless Steel; TEM, Transmission Electron Microscopy; TKD, Transmission Kikuchi Diffraction; XCT, X-ray Computed Microtomography.

* Corresponding author.
*E-mail address:* meysam.haghshenas@utoledo.edu (M. Haghshenas).

[1] Equal contribution

https://doi.org/10.1016/j.ijfatigue.2024.108491
Received 15 March 2024; Received in revised form 3 July 2024; Accepted 6 July 2024
Available online 10 July 2024

**Nomenclature**

| | |
|---|---|
| $\%V$ | Volume percentage |
| $\%wt.$ | Weight percentage |
| $\Delta k_{th}$ | Crack propagation threshold |
| $\sigma_0$ | Material constant representing the friction stress in the Hall-Petch equation |
| $\sigma_y$ | Yield strength of material |
| $a$ | Crack length |
| $a_{in}$ | Initial crack length |
| $C^*$ | The material parameter in Paris law |
| $d$ | The average grain size of the material |
| $f(x)$ | Probability density function |
| $F(x)$ | Cumulative distribution function |
| *F-Value* | The F value in regression is the result of the null hypothesis test |
| $g$ | Murakami's defect coefficient |
| $HV$ | Vickers hardness |
| $K$ | Hall-Petch slope |
| $m$ | The material parameter in Paris law |
| $n$ | Exponent of Murakami's model for crack size correction |
| $R$ | Stress ratio |
| $Y$ | Linearized Gumble Variate |
| $\alpha$ | The exponent of Murakami's model for stress ratio |
| $\beta$ | Scale parameter of Gumble distribution |
| $\mu$ | Location parameter of Gumble distribution |
| $\sum 3$ | Sigma 3, grain boundary with misorientation angle between neighboring grains around $70.53^{\circ}$ |

of surface effects [3,4]. Indeed, rotating bending corrosion fatigue (RBCF) testing allows for the precise evaluation of surface effects induced by manufacturing processes, mechanical stresses, and corrosive environment (e.g., manufacturing defects and surface corrosion pitting), offering invaluable insights into the material's susceptibility to fatigue-induced failure and corrosion-related degradation in marine environments. To this end, investigating the RBCF behavior of AM materials (e.g., stainless steel) holds dominant significance for marine, shipbuilding, naval, and naval aviation applications [5,6].

AM'd materials exhibit notably reduced fatigue lifetimes (in the RBF test) and lower strengths in high-cycle fatigue regimes (HCF) when compared to the wrought counterparts [4,7,8]. According to Shrestha et al. [4,8], in parts subjected to RBF, the stress distribution is non-uniform across the specimen, with surface roughness and the spreading of volumetric defects in AM'd components exerting a notable influence on stress intensity factor and the fatigue resistance of AM parts. In a recent study on carburized SS 316L conducted by Liu et al. [9,10], it was reported that fatigue behavior exhibited a high degree of dependency on alterations in surface characteristics induced by temperature elevations during the RBF testing. Like other alloys, the presence of gas porosities and sub-surface non-metallic inclusions in AM'd materials would likely correlate with microstructural variations under severe environmental conditions [11,12]. Consequently, the interplay between phenomena influenced by harsh environmental conditions and the surface properties of the material under stress gradients in RBF could lead to a competitive crack initiation process. According to Shrestha et al. [4,8] and Liu et al. [9,13] research on AM'd and conventionally manufactured (CM'd) SS 316L, surface defects and roughness, alongside alterations in surface quality in harsh environments, may be identified as the primary factors contributing to the reduced fatigue strength observed in AM'd specimens when compared to CM'd counterparts.

Researchers have extensively studied the corrosion behavior of AM'd SS 316L [14–16], however, our comprehension of this phenomenon is constrained by the lack of studies examining the combined influences of corrosion and fatigue, highlighting the need for further research in this area. The corrosion properties of CM'd SS 316L are significantly impacted by the existence of MnS inclusions and much larger chromium depletion zones. These factors are recognized for their ability to impair the passive layer, thereby encouraging localized corrosion, specifically pitting corrosion [17,18]. In contrast, the majority of nanoscale oxide inclusions in AM'd SS 316L are composed of Si, Al, Mn, and Cr [19,20]. These elements do not significantly impair the resistance to pitting corrosion [20]. The insignificance of carbide precipitation in SS 316L stems from the alloy's exceedingly low carbon content, rendering it applicable in sectors such as marine, medicinal, and food [21].

Due to variations in the AM process and the properties of the manufactured materials, the comparison of corrosion-fatigue behavior between AM'd and CM'd SS 316L materials remains challenging in the existing literature. Nonetheless, a few researchers have compared the corrosion behavior of AM'd 316SS and CM'd counter material [22–24]. The difference in corrosion resistance of the materials is primarily attributed to the high solidification rates [25] of the AM'd processing, which prevents the formation of non-metallic contaminants such as MnS, which are potent pit initiators [26]. Nie et al. [22] and Chao et al. [27] reported that the passive films on both AM'd and CM'd SS316L are constituted primarily of Cr and Fe oxides and hydroxides. A large quantity of sub-grain boundaries and an extreme dislocation density facilitate the creation of an even denser passive film on AM'd SS 316L than on CM'd SS 316L, resulting in superior general corrosion resistance same as reported by Lodhi et al [28] and Wang et al [29]. However, the AM'd SS 316L passive film contains a minimal hydroxide content, along with the micro-galvanic corrosion influence between the sub-grain boundaries and sub-grains caused by Mo segregation, decreases the self-repair ability of the passive film, resulting in lower pitting corrosion resistance of AM'd SS 316L compared to its CM'd counterpart [30,31]. Some studies [32,33] also highlighted the potential involvement of the fine microstructure produced by the AM which may contribute to a rise in the passive film's intensity, and a reduction in pit penetration.

Several investigations [34–36] have demonstrated that pits could be dangerous in the HCF regime, as crack initiation was observed to occur at these defects. Corrosion fatigue combination may also be especially hazardous for certain materials [37,38]. In the literature, various coupling mechanisms, for instance, local persistent slip bands prompting pit initiation [39], loading drive pit growth morphology [38], corrosion at the crack tip [40], and hydrogen embrittlement [41], have been identified. These coupling mechanisms have the potential to significantly reduce the lifetime more than what would be anticipated if corrosion and fatigue phenomena were evaluated in isolation.

The relationship between pitting and crack initiation is a complex subject, and numerous studies have been conducted [42–44] to investigate the various parameters influencing the transition from pit to crack. For instance, Turnbull [45] suggested that cracking would predominantly occur at the base of corrosion pits due to the heightened stress and chemical aggressiveness in that region [46,47]. The investigation employed advanced imaging techniques, such as X-ray computed tomography (XCT), to accurately depict the three-dimensional morphology of pits and associated cracks. A systematic analysis revealed that a significant proportion of cracks originated from or near the pit mouth, especially under conditions of shorter exposure durations. This finding contests the earlier assumption that fracture initiation is invariably restricted to the pit base. Furthermore, the study examined the mechanisms of crack initiation, proposing that the observed phenomenon is due to the coalescence of cracks near the pit mouth, followed by their accelerated propagation.

The properties of AM'd SS 316L under stress corrosion cracking or corrosion fatigue conditions have been the subject of a limited number of investigations. For nuclear applications, Lou et al. [48,49] examined the stress corrosion crack growth behavior of AM'd SS 316L in high-temperature water. Anisotropic crack growth behavior was observed, which was contingent upon the direction of crack propagation concerning the build orientation. The corrosion fatigue behavior of CM'd and AM'd SS 316L was initially assessed by Gnanasekaran et al. [50] using fatigue tests conducted in both air and a 0.6 M NaCl solution ($R = 0.1$, $f = 20$ Hz). The authors verified that the CM'd material had a higher rate of pitting formation on its surface, hence serving as an initiator for crack initiation. In contrast, the AM'd material did not exhibit this characteristic. The crack growth experiments reveal that the AM'd material exhibits reduced rates of crack growth in a NaCl solution, particularly when tested at a frequency of 2 Hz instead of 20 Hz.

Merot et al. [15] employed potentiodynamic polarization to induce pits on the surface of the examined specimens of AM'd SS 316L. They compared the impact of these pits on the fatigue behavior of specimens with electrical discharge machined (EDM) surface defects and those with a polished surface. The fatigue characteristics were characterized by employing Murakami's $\sqrt{area}$ parameter, and no statistically significant variations were observed. They reported that the defect morphology of pits, EDM defects, or absence of fusion defects does not appear to have a substantial impact on the onset of cracks. Stern et al. [51] discovered through their investigation of the corrosion-fatigue characteristics of AM SS 316L, utilizing a uniaxial test machine, that elevated nitrogen content in AM SS 316L results in enhanced corrosion performance. This enhancement is evidenced by improved polarization curves and superior corrosion fatigue behavior compared to unmodified AM SS 316L. The application of a fracture mechanical approach provides the characterization of the defect-dominated fatigue life in both air and 0.6 M NaCl solution. Stern et al. [51] reported there was no statistically significant distinction observed in the fracture surfaces of specimens subjected to testing in a 0.6 M NaCl solution as opposed to those examined in air. Crack-initiating defects were identified as those located either directly on or slightly below the surface of the specimens. The absence of corrosion products can be attributed to the rapid re-passivation of crack surfaces, which prevented any further corrosion. Trans-granular propagation was observed in nearly all cracks, resulting in the formation of fan-shaped patterns, as documented by Shaikh et al. [52]. Nevertheless, pitting did not adversely affect any of the specimens, as crack initiation was predominantly attributed to process-induced defects.

Maruyama et al. [53] reported certain secondary cracks emanating from the pits under the synthetic body fluid test of CM'd SS 316L which was close to the finding by Stern et al. [51]. Hashim et al [34] reported that the failure rate of corrosion pits decreased as the aspect ratio (the ratio of depth to width) increased. Crack initiation occurred at the base of shallow pits, transferred to the shoulder of quasi-symmetrical pits, and culminated at the mouth of deep pits. Finite element analysis from their work revealed that local stress at the base of the pit became compressive as pit depth increased due to higher stress concentration factors while the loading condition was tension mode.

Considering the provided literature review, the impact of pit formation on surface quality, and by extension, crack initiation, and fatigue characteristics, is critical and intricate. The mechanisms that cause pits to crack are subject to the control of numerous factors and facets, which necessitates thorough investigation. Given that corrosion is a progressive surface phenomenon and that AM metals often possess surface defects, examining imperfections such as pits or AM defects can enhance our understanding of the relationship between corrosion and fatigue. Conversely, the scarcity of research on the corrosion-fatigue characteristics of AM'd SS 316L alloy underscores the need to investigate the impact of surface pitting on the material's durability and the initiation of cracks from surface AM defects or pits. The objective of this investigation is then to assess the ex-situ corrosion-fatigue performance of AM'd (i.e., laser powder bed fused) SS 316L when subjected to rotating bending stresses. The investigation will be conducted at room temperature, considering two distinct environments: ambient air and corrosive solution. Pre-corroded specimens will be utilized to assess the influence of pitting and hydrogen embrittlement. Furthermore, a prediction model for fatigue strength will be established by integrating fractography results with Murakami's models. It is worth noting that the rotating bending corrosion fatigue behavior of AM 316L is crucial for maritime and naval applications due to the unique challenges posed by marine environments, including saltwater exposure and fluctuating mechanical stresses. Without a comprehensive understanding of how corrosion and fatigue interact in such conditions, the structural integrity of components could be compromised, leading to costly failures, safety hazards, and operational disruptions in maritime and naval operations.

## 2. Experimental procedure

### 2.1. Materials and specimen fabrication

Test specimens were fabricated using laser powder bed fusion (LPBF) with SS 316L powder with the chemical composition as Fe (base)-17.0 wt% Cr-13.0 wt% Ni-2.5 wt% Mo. Specimens resembling a dog bone (Fig. 1(a)) made of SS 316L, measuring 160 mm in length, 6.5 mm in gauge diameter, and 11 mm in shoulder diameter, were fabricated utilizing a GE M2 concept laser machine within a nitrogen-purged environment. The manufacturer's default print parameters were employed (see Table 1). Following stress-relief heat treatment in a furnace at 550 °C for 6 h, the printed specimens were subsequently cut using an electron discharge machine (EDM). The employed thermal treatment is a common way to relieve the residual stresses which could affect the local mechanical properties, particularly in the RBF test where surface quality and condition are critical; by the same token, fatigue performance can be significantly impacted by residual stress [54,55]. Additionally, localized regions of high-stress concentration may be produced by residual stress, which may increase the corrosion susceptibility of AM components [56,57]. Therefore, post-fabrication stress relief treatment was applied to facilitate the homogenization of stress distribution within the material, thereby reducing the likelihood of corrosion initiation and propagation. To mitigate unforeseen effects and minimize experimental errors, stress relief was performed on the printed specimens in this study. The density of the printed specimens was measured using the Archimedes method, yielding a relative density of 99.3 % ± 0.07.

The dog bone printed parts depicted in Fig. 1(a) were separated from the built plate and machined to a uniform gage section using a computer numerical control (CNC) lathe following ISO 1143 [58]. These specimens with the geometry depicted in Fig. 1(b) were further polished with sandpapers of varying grits until the 5000 girt number. To examine the mechanical properties and microstructure, four identically printed rods were machined and subjected to a tensile test. These rods with a length of 100 mm and a diameter of 10 mm were printed for tensile testing (Fig. 1(c)). The printed rods were machined into the standard tensile test specimen based on the ASTM E8 standard , and their geometry is shown in Fig. 1(d).

### 2.2. Pre-corrosion setup

To conduct corrosion tests, we utilized a 30 % HCl solution as the corrosive environment for ten days. As shown in Fig. 2(a), machined specimens (Fig. 1(b)) were suspended in the corrosive media at room temperature for ten days. To prevent corrosion of the shoulder sections, impermeable polymeric tape was used (i.e., only the gauge section of the specimens exhibited corrosion, as shown in Fig. 2(b). A witness specimen was employed to compare the surface quality of the material before and after corrosion using optical microscopy. The witness specimen was a rectangular specimen of the same material under identical corrosion conditions (Fig. 2(c)).

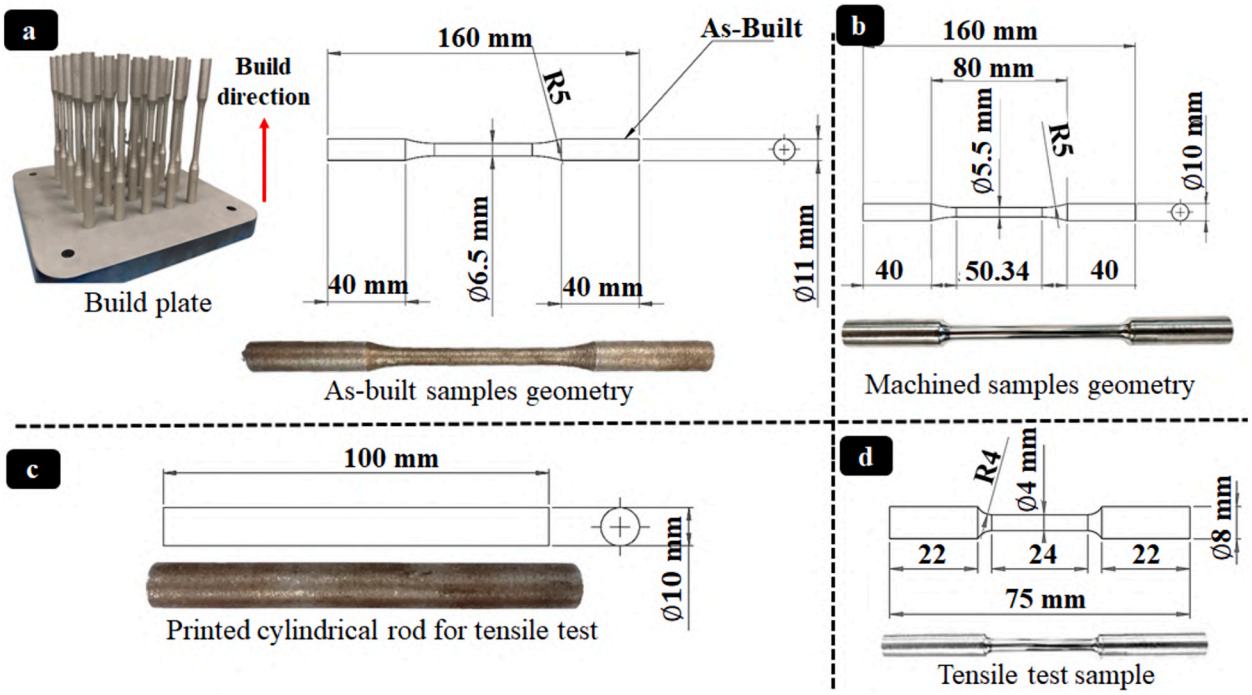


**Fig. 1.** a) as-built dog bone specimens and additively manufactured built plate, b) machined specimens geometry based on ISO 1143, c) printed cylindrical rods for tensile test, d) tensile test standard specimen's geometry based on ASTM E8.

**Table 1**
Printing parameters employed to print the studied LPBF SS 316L.

| Power (W) | Speed (mm/s) | Spot size (μm) | Hatch space (μm) | Layer thickness (μm) |
|---|---|---|---|---|
| 370 | 1350 | 130 | 90 | 50 |

### 2.3. Microstructure and defect analyses

To evaluate the microstructural aspects of the printed specimens, the mid-section of the LB-PBF SS 316L cylinder-shaped rods was cut along the plane perpendicular to the built plate. To attain a mirror-like finish, the cut specimens were hot-mounted, ground with sandpaper of varying grits, and polished with a suspension of 9 $\mu m$ polycrystalline diamonds and colloidal silica. Following ASTM Standard E407:07 [59], a solution of 4 g $CuSo_4$ + 20 ml HCl + 20 ml distilled water was used to etch the polished specimens. The electron microscope is equipped with the latest Oxford Electron backscatter diffraction (EBSD) Symmetry® S3 detector, which utilizes cutting-edge CMOS sensor technology. The incorporation of this detector alongside the AZtecHKL software enables thorough analyses of EBSD and transmission of Kikuchi diffraction (TKD) EBSD.

To evaluate the internal structure of the specimens a computed tomography inspection has been exploited. The custom-built XCT equipment that has been used belongs to the Interdepartmental Centre J-Tech@PoliTO inside Politecnico di Torino (Fig. 3). The facility is equipped with an X-ray tube of 50 W and a minimum focal spot size of 5 μm.

The specimens have been inspected in the central zone. The parameters used for the XCT are 260 kV and 80 μA which give an X-ray power of 20.8 W. Using an X-ray source–specimen distance of 50 mm and an X-ray source-detector distance of 1200 mm and 8.3 μm spatial resolution has been reached. For each specimen, 1600 projections have been acquired and the 3D volume reconstructions have been performed

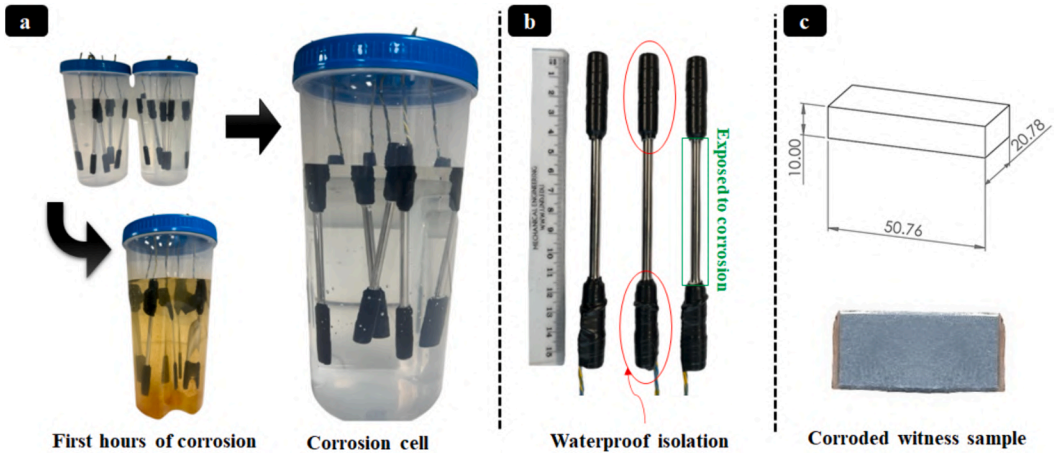


**Fig. 2.** a) corrosion media cell containing suspended specimens; b) specimens prepared for corrosion testing through impermeable isolation in shoulders; and c) witness specimen geometry and an actual specimen for studying the corrosion effect on surface degradation.

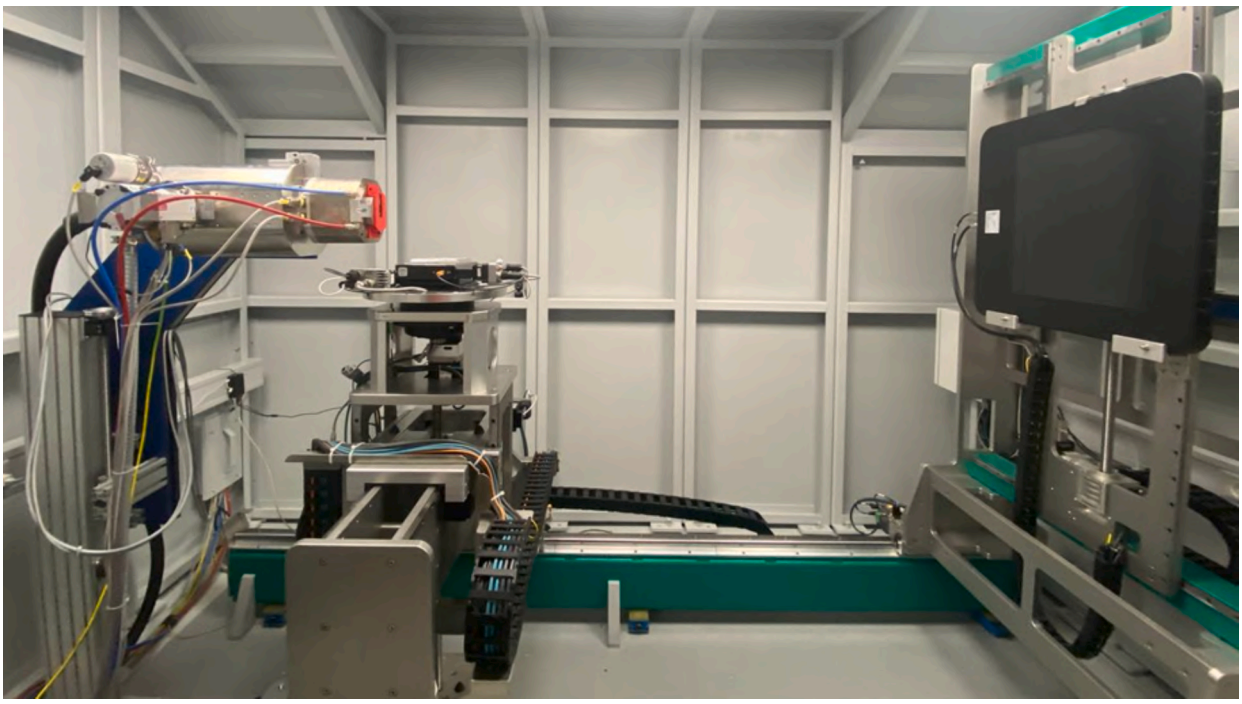

**Fig. 3.** Custom-built tomography equipment in J-Tech @PoliTO.

through VG MAX 3.5 software (Volume Graphics GmbH, Heidelberg, DE) using a filter back projection algorithm. The specimen to be investigated is made from steel, which is a quite dense material, to enhance the final quality of the tomography a physical filter of 0.8 mm of Cu has been used, to filter out the low-intensity radiation and reduce noise in the post-processing reconstructions.

The VG Studio inclusion/porosities module was used to characterize the defects distribution. The software algorithm determines if a reconstruction voxel is a void or specimen material by setting a grayscale threshold. Black voxels commonly depict air around or voids within a material in 3D reconstruction. Voids in the material are lit by the surrounding substance. Thus, a threshold value that lets the software distinguish voids from artifacts was carefully chosen. The software may classify projection noise artifacts as defects. These artifacts usually surfaced. Therefore, a minimum distance of 30 μm between a suspected defect and the specimen's surface has been defined to filter out these inaccuracies. Localized and geometrically defined defects are detected in the specimen. This study focuses on equivalent diameter and sphericity. The first parameter is the diameter of a sphere with the same volume as the defect, and the second is the ratio of its surface area to the defects. To accurately assess the impact of corrosion on the surface quality of the pre-corroded sample, a profilometry analysis was conducted using the Taylor Hobson Intra Touch 3D Profilometer. This analysis was necessary to filter out surface artifacts that were present during the CT scan analysis.

### 2.4. Tensile and hardness testing

To ascertain the initial stress level for the fatigue test and investigate the mechanical properties, uniaxial tensile assessments were performed utilizing an Instron 8822-servo hydraulic test frame outfitted with a 25 kN load cell. To quantify and regulate the axial deformation of the specimens, a 20 mm gage length Epsilon 3542 extensometer was utilized. Notably, the quasi-static tensile experiments were conducted in compliance with ASTM Standard E8 [60] by setting the strain rate at 0.001 $s^{-1}$.

The hardness test was conducted to look at how corrosion processes affect hardness on the surface and how cyclic loading affects local work hardening below the fracture surface. Specimens were cut for this purpose (see Fig. 4), and nano-indentation equipment was used to examine both the pre-corroded and non-corroded fractured specimens. A nano-indentation platform (iMicro, KLA Instruments) was used to conduct the small-scale mechanical testing. In this investigation, the indentation positions were chosen using a methodical grid methodology. Every indent in the grid had a defined distance from the next in regular spacing as recommended per ISO 14577 [61]. A 400 × 400 $\mu m^2$ area was efficiently covered by a 3 × 3 array of indents, with a 100 μm gap between each indent. A Berkovich indenter (probe), with a 100 nm tip radius, was used and a constant load of 500 mN and a loading/unloading rate of 25 mN/s were applied to each specimen, yielding 25 indents. On every specimen, the indentations were methodically placed in a grid pattern.

### 2.5. Fatigue testing and postmortem characterization

To assess the impact of surface quality on pre-corroded and non-corroded specimens, RBF testing was employed. The Zwick Amsler RBM120T machine was employed at ambient temperature to conduct fatigue tests on the pre-corroded specimens. The stress amplitude levels in this experiment ranged from 420 (corresponding to 86 % yield strength) to 203 MPa (40 % yield strength). To prevent self-heating, the frequency was maintained at 1000 rpm (16.7 Hz), and the test was carried out following ISO 1143 [58]. A four-point cantilever RBF was utilized to maintain a constant momentum across the entire gauge section of specimens, with the neutral axis of the specimens experiencing the least tension and the surface the highest. The principles of this apparatus and the equation for converting momentum to stress are illustrated in Fig. 5(a). The apparent (Fig. 5(b)) decrease in stress gradient from its maximum at the surface to zero along the neutral axes presents a potential avenue for examining the impact of surface quality on fatigue characteristics (Fig. 5(c) shows the Zwick Amsler RBM120T system).

To explore the fracture surface and determine the location of crack initiation, propagation, and final fracture using statistical models, we conducted SEM-based systematic fractography. EBSD was also employed to capture intricate microstructural details in fatigue and tensile specimens for the most comprehensive investigation of the

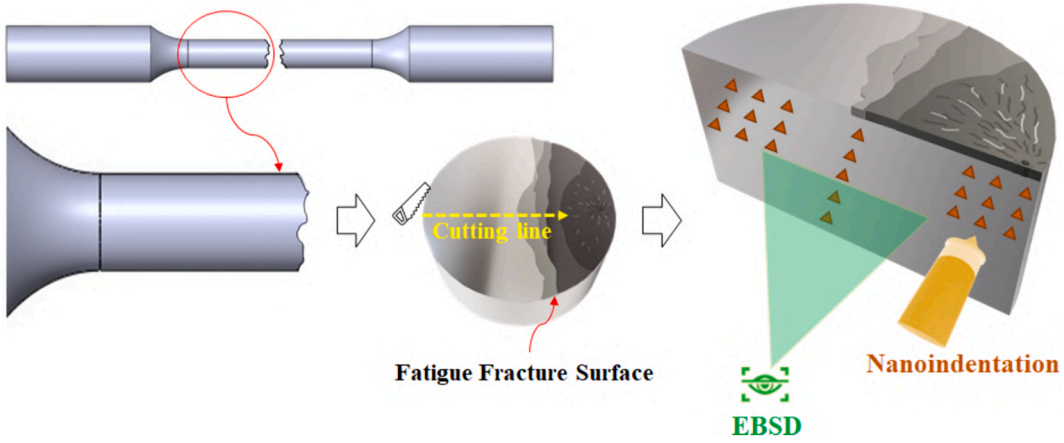


**Fig. 4.** Schematic of preparation procedure of fractured specimens for the EBSD and depth-sensing (instrumented) indentation tests.

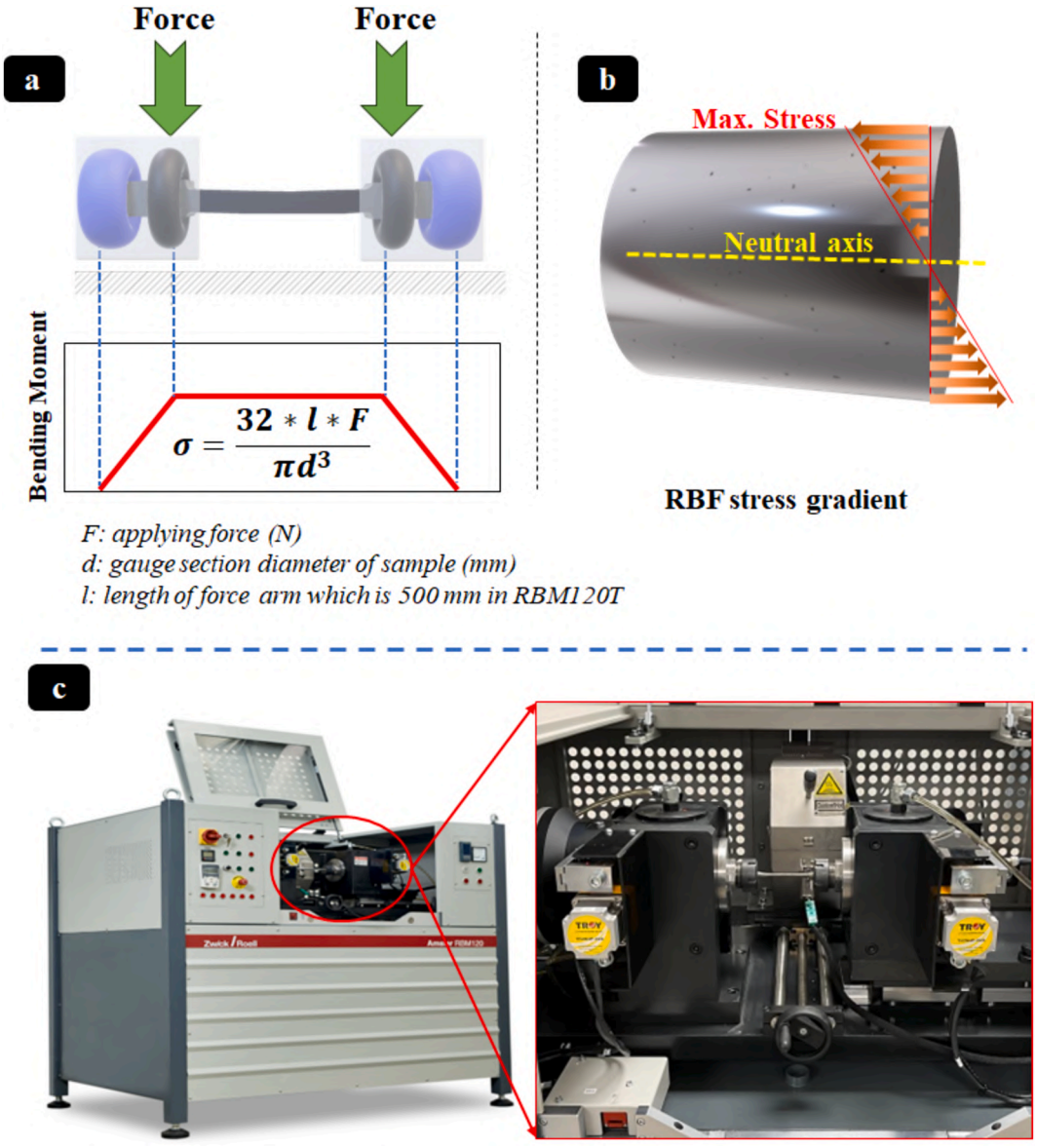


**Fig. 5.** a) the schematic of the 4-cantilever RBF machine and the constant momentum diagram on the whole gauge section; b) the stress gradient from the maximum on the surface through the zero in the neutral axis; c) Zwick RBF testing machine and specimen set up used in this study.

fracture surface and the impact of cyclic loading on grain sizes and microstructure alterations beneath the fractured surface (Fig. 4). Moreover, the EDS technique was employed to evaluate the impact of corrosive solutions (particularly $Cl^-$ and corrosion precipitates) on the corroded specimens. For modeling and to determine the impact of defects on the initiation of cracks, statistical distribution diagrams for surface and interior defects were generated using X-ray computed microtomography (XCT or μ-CT) apparatus.

### 2.6. Fatigue life prediction

For modeling of a lifetime, the experimental data (e.g., S-N) were assessed using the Analysis of Variance (ANOVA) method to verify that the obtained values align with the statistical foundation and that our data are valid. Following this, we utilized factorial design to verify the fatigue life model that adhered to the traditional Basquin model [62] for fatigue life prediction. ImageJ software estimated defect size following mathematical modeling based on statistical data of the S-N curve for micro-scale investigation of fatigue modeling. Fractography data were utilized in the Murakami model [63,64] and Paris law [65] to examine crack propagation.

## 3. Results and discussion

### 3.1. Microstructural analyses

Fig. 6 illustrates the OM and EBSD micrographs of the as-built material (with a relative density of 99.3 % ± 0.07). One can observe the superposition of a melt pool and elongated grains that are aligned parallel to the building direction (BD) (Fig. 6(a)). As illustrated in Fig. 6(b), the EBSD results indicate that the grain orientation is nearly random and that no texture is preferred. Additionally, it is evident that internal

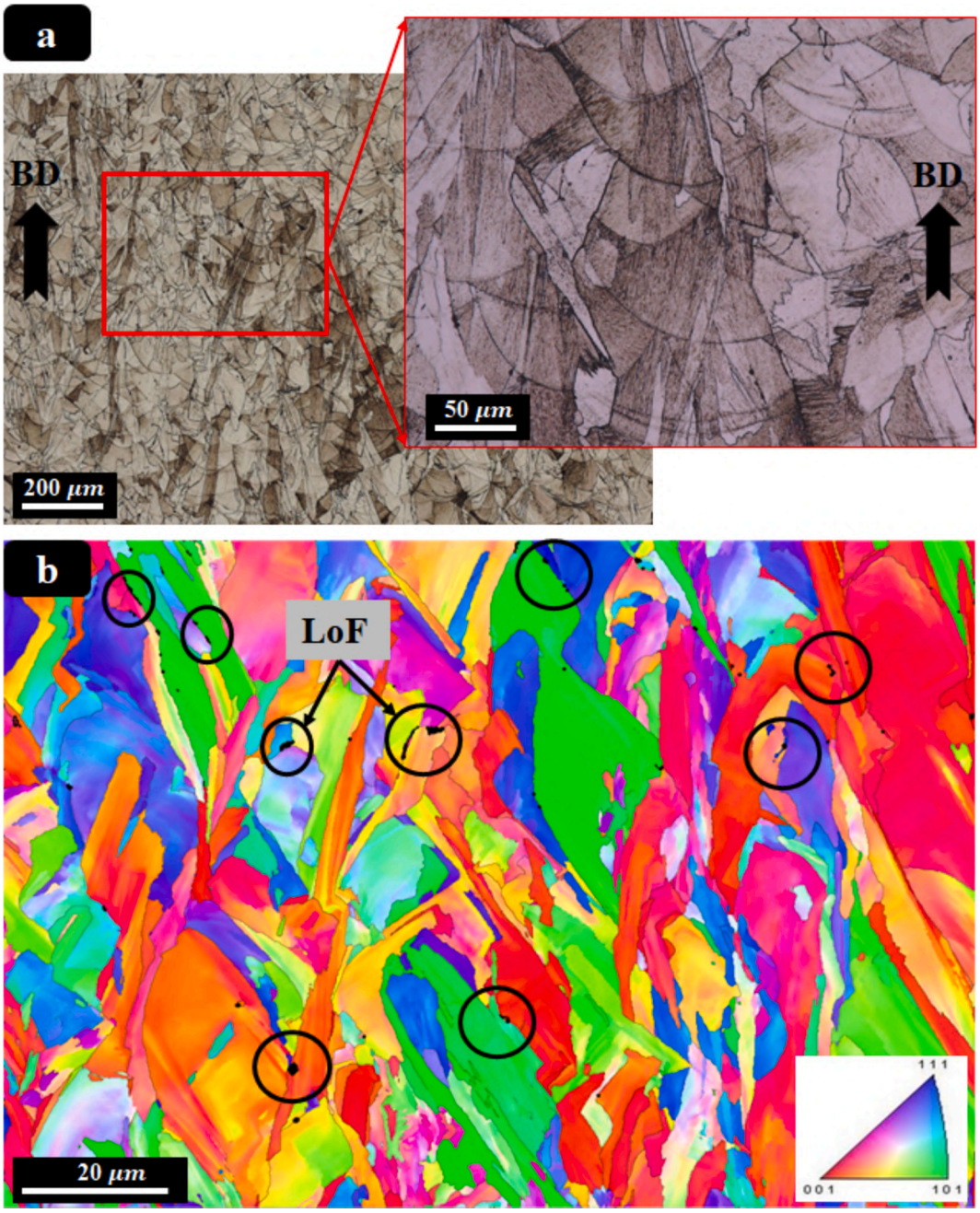


**Fig. 6.** a) optical microscopy images of the etched specimen, b) non-preferred microstructure EBSD image with some LoF at grain boundaries.

defects, including pores and lack of fusions (LoFs), are located at the grain boundary.

Fig. 7 depicts the witness specimen used in the corrosion investigation, which was subjected to a 10-day corrosion process in a 30 % volume concentration of HCl. The studied LPBF SS 316L specimens exhibit extensive surface degradation characterized by pronounced crevices and pits, signifying the substantial influence of the corrosive medium on surface integrity. The high concentrations of $Cl^-$ and $H^+$ ions in the 30 % HCl solution result in severe surface corrosion, as depicted in Fig. 7(c-e). The boundaries of the melt pools have entirely vanished after corrosion and only very ambiguous lines in Fig. 7(d) & (e) can be indicated. The growth direction of the corrosion crevices is obscured, but it appears that the corrosion originated from a surface defect or discontinuity, such as the boundary of the melt pools, and then continued preferably through the melt pool's boundaries. It appears that in corrosive media, where a high concentration of $H^+$ was present, anodic dissolution and the formation of a passive layer occurred very rapidly. However, the passive layer could not prevent corrosion in this high-potential corrosive media. The electrochemical dissolution of the passive film that forms on the gas pore surface is responsible for pitting nucleation in LPBF SS 316L [66]. The strength of the dissolution is influenced by the carrier density and/or the space charge layer of the passive film. The schematic representation of the space charge layer that develops at the interface between the passive film and electrolyte, as determined by the Mott-Schottky [67,68] measurement and the energy band theory of the semiconductor [69], is schematically illustrated in Fig. 7(f). The presented schematic demonstrates how the potential difference at the interface relating the electrolyte and base metal induces conduction and values in the band potential. This potential difference serves as the driving force behind corrosion phenomena. As the schematic may appear, the passive layer functions as an isolation barrier, controlling electron migration from the electrolyte to the metal layer. When the concentrations of $H^+$ and $Cl^-$ ions are significantly higher, the Helmholtz layer will be more significant and powerful. As a result, the space charge layer will be charged more to maintain equilibrium in the system. As a result, the potential variation will exceed the stability of the passive layer, leading to localized corrosion and, in certain areas, desolation of the passive layer. Consequently, the crevice pattern of corrosion depicted in Fig. 7(c-e) is anticipated.

The surface area affected by pitting was quantified in Fig. 8 utilizing an image processing methodology; the calculated area for various magnifications indicates that the pitting on the surface is approximately 12 % ±0.5. This implies that while the corrosion is localized, the locations of corrosion were dispersed at random across the surface, and the pitting area at a large scale (encompassing the entire surface, as shown in Fig. 8(a) mirrored the tiny, magnified region of the specimen under increased magnification. Therefore, we rely on the findings from the witness specimen to infer the extent of surface pitting in the remaining corroded fatigue specimens. It is reasonable to deduce that all specimens experienced a surface pitting of approximately 12 % ±0.5. Additionally, it is critical to note that these results are at the microscale; the maximum magnification of the measurements is X200 in Fig. 8(c) indicating that the image processing was incapable of detecting the crevices at the smaller scale. The surface area (12 %) of corroded sites that have been calculated may serve as an indicator of the surface quality degradation caused by corrosion, a topic that will be further explored in the fatigue results section.

### 3.2. CT-scan and internal defect distribution analyses

In this Section, a detailed defect analysis is carried out. Figs. 9 and 10 compare the distribution of defects within the cylinder volume (the transparent grey area), Fig. 9 for the Non-corroded specimen, and Fig. 10 for the Pre-corroded specimen. By analyzing the control volume, surface corroded fissures are visible, and the surface of the pre-corroded specimen exhibits asperities (Fig. 10), whereas the surface of the non-corroded specimen is nearly smooth (Fig. 9). Although the primary and common objective of the CT scan is to analyze volumetric defects induced by LPBF in the microstructure, Fig. 10 reveals surface waviness (roughness) caused by corrosion in the pre-corroded specimens (relative to the smooth surface finish of the non-corroded specimens, Fig. 9. The CT scan results indicate that the 10-day exposure to the corrosive environment largely affected the surface, leaving interior defects largely unaffected.

For the internal defect analysis, the equivalent diameter, $D_e$, has been considered since it is correlated to the defect volume and allows the comparison of defects with different and irregular morphologies. The colors associated with the defect $D_e$ provide indications on the defect size, with the majority of defects characterized by $D_e$ smaller than 100 μm (green color) and with a limited number of bigger defects (red defects), with $D_e$ up to 141 μm for the Pre-corroded specimens and up to 113 μm for the non-corroded. This difference is quite limited and can be considered within the large scatter of defect size typical of AM'd specimens.

To further investigate and improve the accuracy of CT-scan results in data analysis concerning surface filtering distance, we assessed the impact of surface artifacts on CT results. Consequently, the following section examines the impact of a non-filtering 30-μm distance on CT scan results. Subsequently, profilometry analysis was employed to further investigate the surface effect.

In Fig. 9(a), an increased number of surface defects are visible, while in Fig. 9(b), an enlargement of the surface reveals that these defects are merely artifacts, not actual defects. These artifacts result from the beam hardening phenomenon. Beam hardening is a characteristic of tomography analysis when dealing with heavy and dense alloys such as steel, where the internal volume of the material appears brighter and the surface darker. Since the defect analysis algorithm relies on contrast differences between voids and material, these darker surface shadows can lead to false defect detections.

In Fig. 10(a), the defect analysis results for the pre-corroded specimen are shown, and in Fig. 10(b), an enlargement of the surface highlights some characteristic artifacts. Therefore, it should be noted that removing the edge distance limitation in the analysis does not change the overall defect detection but introduces numerous small surface artifacts. These artifacts arise from the limitations of tomography analysis with heavy and dense materials like steel. However, despite excluding the surface from the defect analysis, the increase in surface roughness is still clearly visible (Fig. 11).

#### 3.2.1. Extreme value distribution analysis of porosity

The Type 1 Largest Extreme Valued Distribution (LEVD), commonly referred to as the Gumbel distribution, has been used to analyze the most critical defects of pre-corroded and non-corroded specimens, i.e., the upper tail of the distribution of defects controlling the fatigue response. To estimate the parameters of the LEVD, block maxima sampling has been employed, starting from the defect-equivalent diameters $\boldsymbol{D_e}$ assessed with micro-CT inspections. More in detail, the inspected volume has been discretized into 10 cylinders with equal volume. For each sub-volume, the $\boldsymbol{D_e}$ of the largest defect has been recorded. The parameter estimation has been implemented by applying the Least Square Method, to estimate the location $\boldsymbol{\mu}$ and the scale parameters $\boldsymbol{\sigma}$ of the LEVD, whose cumulative distribution function (cdf) is reported in Eq. (1):

$$\boldsymbol{F(x) = \exp[-\exp\left(-\frac{x-\mu}{\sigma}\right)]} \tag{1}$$

being $\boldsymbol{x}$ the characteristic defect size, considered as the equivalent diameter $\boldsymbol{D_e}$ in the following analyses. Eq. (1) can be linearized, according to Eq. (2), to obtain the reduced variable $\boldsymbol{Y}$:

$$\boldsymbol{Y = -\ln(-\ln(F(x)))} = \frac{\boldsymbol{x-\mu}}{\boldsymbol{\sigma}} \tag{2}$$

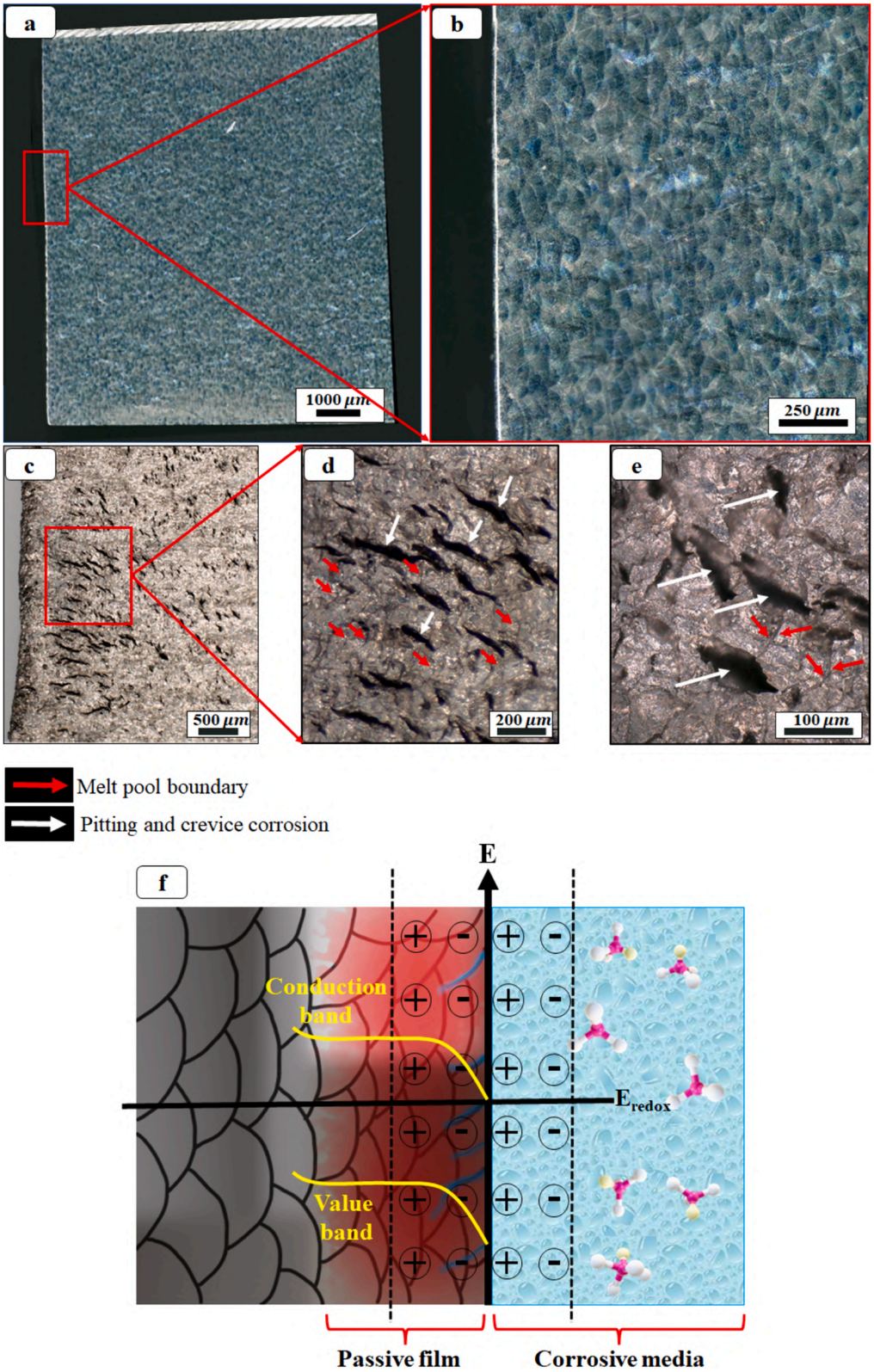


**Fig. 7.** a & b) the OM images of the witness specimen before the onset of the corrosion process; c, d, & e) OM image of the corroded specimen surface after a 10-day exposure to HCl 30%V (red arrows indicating ambiguous melt pool boundaries and white arrows indicating pitting), e) the corroded surface with pits measuring less than 100 um, f) schematic of passive layer formation in corrosive environment.

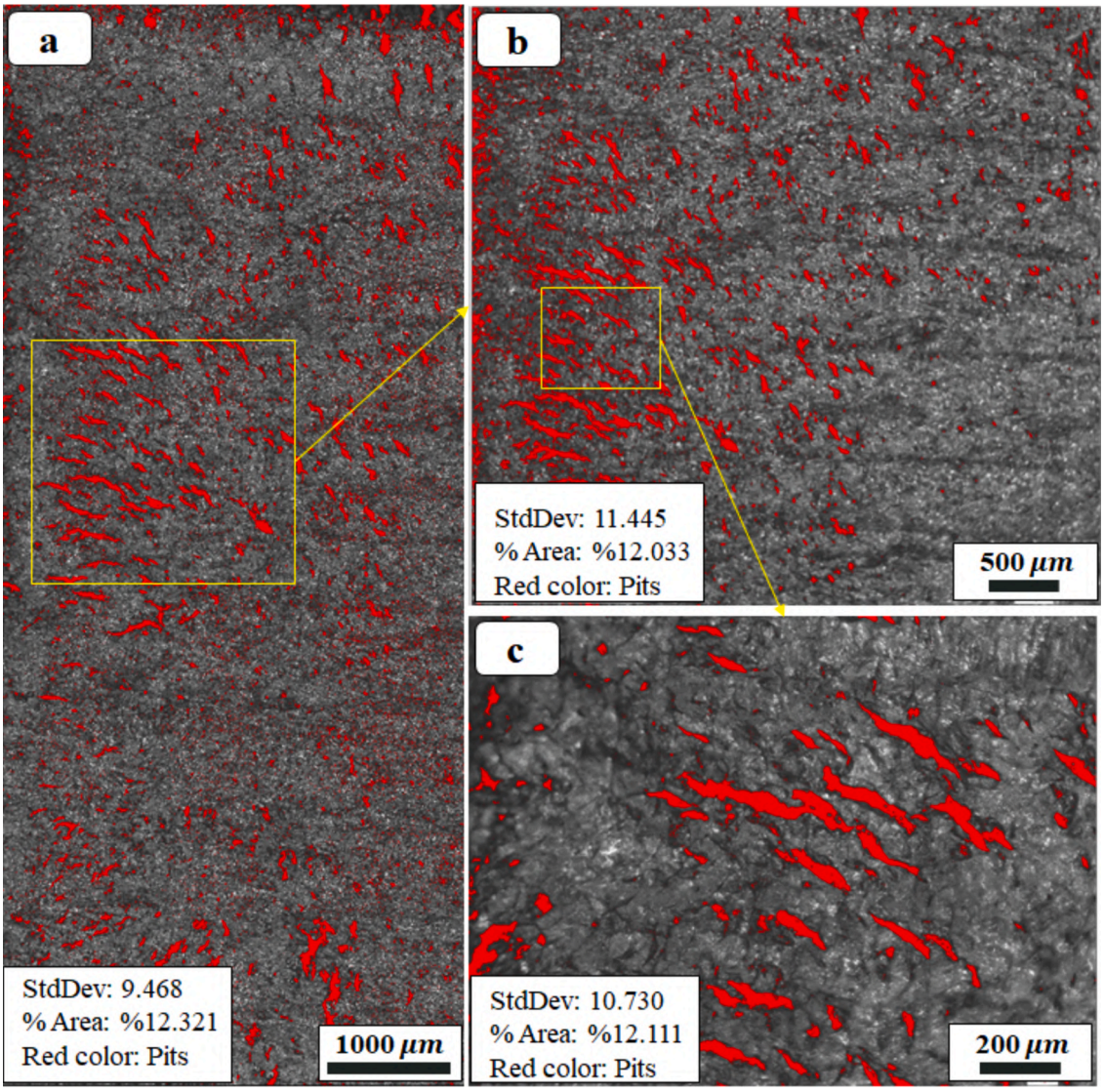


**Fig. 8.** a) the corroded surface in 50X magnification with 12% of the corroded area, b & c) the selected area in 100X and 200X magnification respectively.

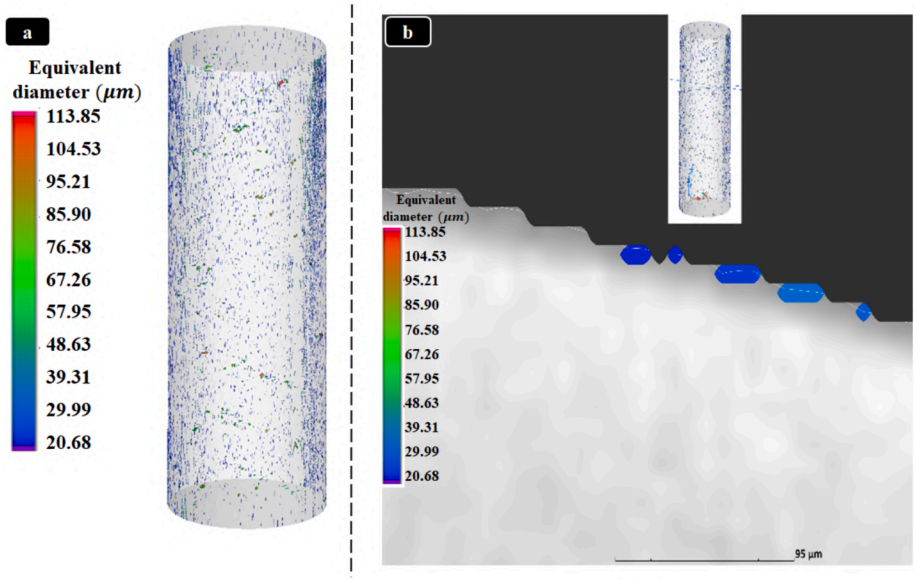


**Fig. 9.** a) Defect analysis with no edge distance filtering and b) surface artifacts of the surface of the specimen.

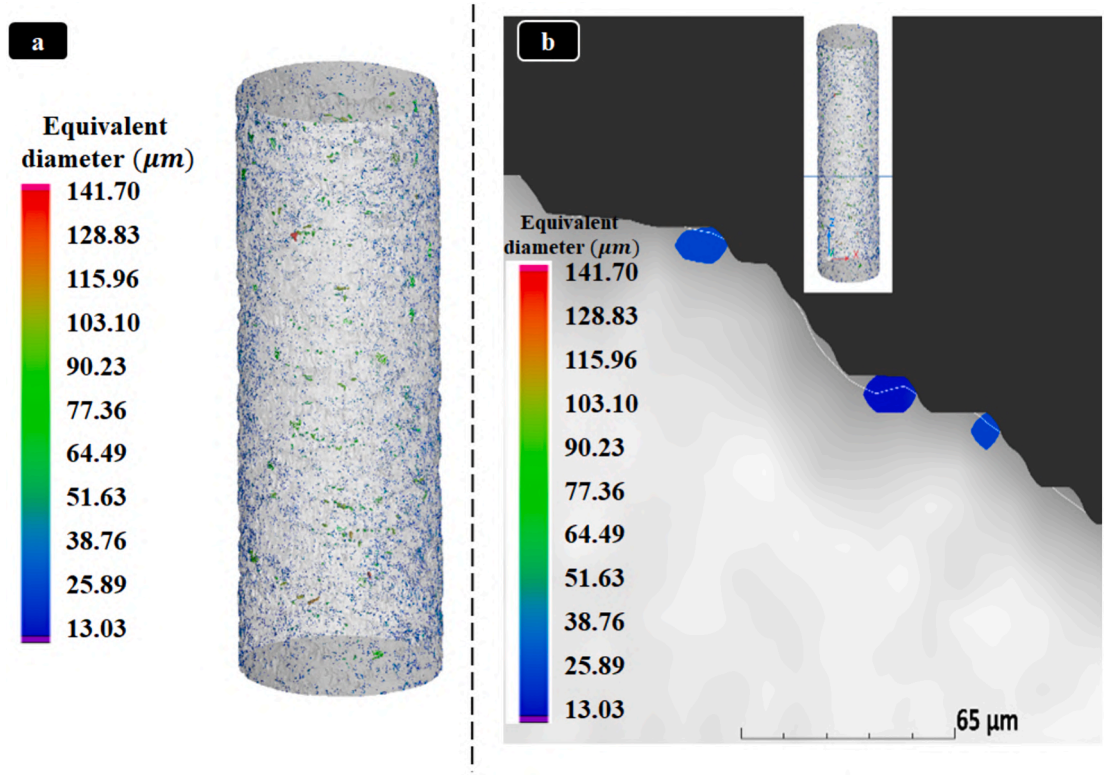


**Fig. 10.** a) Defect analysis with no edge distance filtering and b) surface artifacts of the surface of the specimen.

Fig. 12(a) shows the defect-equivalent diameters $D_e$ in a Gumbel plot, together with the estimated LEVD, for the Pre-corroded and the Non-corroded specimens. According to Fig. 12(a), the defects are characterized by $D_e$ very close, apart from two large defects in the Pre-Corroded volumes, which influence the trend of the LEVD. However, the different trend is not caused by the corrosion process since this phenomenon is not expected to influence internal defects. To prove this, the same analysis has been carried out by removing the two largest defects in the Pre-corroded specimens: the resulting Gumbel plot is reported in Fig. 12(b). According to Fig. 12(b), the difference between the experimental defects is reduced, with a very similar LEVD trend. To conclude, internal defects are not influenced by the corrosion process and the occurrence of very large and critical defects can be mainly attributed to the large variation and scatter of defects in Additively Manufactured parts. On the other hand, the influence of the corrosion process is visible by analyzing the external surfaces of the inspected Pre-corroded and Non-corroded volumes, and this is expected to influence the fatigue response, as discussed and investigated in the following sections.

### 3.2.2. *Surface roughness analysis by profilometry*

To better evaluate the change in the roughness of the pre-corroded sample and the effect of corrosion on surface quality, a profilometry analysis was conducted using the Taylor Hobson Intra Touch 3D Profilometer. Fig. 13 shows the profiles obtained from the profilometry analysis. Specifically, Fig. 13(a) presents the profile of the non-corroded sample, while Fig. 13(b) displays the profile of the pre-corroded sample. Both profiles measured are 10 mm in length. By analyzing these surface profiles, the roughness parameters listed in Table 2 were extracted.

The results in Table 2 demonstrate that the pre-corroded sample exhibits significantly higher roughness values compared to the non-corroded sample, indicating a substantial increase in surface roughness due to corrosion. The CT-scan and profilometry study revealed that the CT-scan results were nearly identical concerning internal defects, suggesting that the discrepancy in fatigue behavior is primarily due to surface conformity. In contrast, the profilometry results showed a substantial disparity between the non-corroded and pre-corroded specimens, which is attributed to the effects of corrosion. This paper assesses the impact of corrosion on fatigue life in both corroded and non-corroded conditions. The magnitude of the corrosion effect and the associated surface roughness parameters will be the focus of future studies.

### 3.3. *Quasi-static (tensile test) behavior*

The tensile test findings of the studied LPBF SS 316L in its uncorroded state are depicted in Fig. 14. Four tensile tests were conducted on the standard specimens, as depicted in Fig. 1(d), with Fig. 14(a) illustrating the corresponding experimental outcomes. The flow curve depicted in Fig. 14(b) was accomplished by averaging four experimental tensile diagrams. The calculated Young's modulus and yield stress (0.2 % offset stress) were determined to be 182 ± 8.2 GPa and 489 ± 15.5 MPa, respectively. These values are reasonably consistent with the findings reported by Shrestha et al. [4,8] and Merot et al [15,70].

### 3.4. *The effect of corrosion on fatigue behavior*

Fig. 15 depicts the S-N data of the pre-corroded specimens (ex-situ corrosion RBF life) and the virgin (non-corroded specimens). As seen, corrosion tangibly affects fatigue performance (lowers fatigue strength). The fatigue limit for pre-corroded specimens is estimated to be 203 MPa, compared to approximately 242 MPa for non-corroded specimens. The disparity between the two S-N curves indicates a difference of over 40 % in fatigue life between the two specimen groups. The dispersed data in the HCF regime ($10^4$ to $10^6$ cycles) is consistent with the notion that crack initiation from surface defects serves as the primary fatigue mechanism controller. By reducing the stress level to the range of 388 to 356 MPa, the lifetime of pre-corroded specimens decreased by about 70 % compared to non-corroded specimens. For example, the lifetime of a non-corroded specimen at 388 MPa was 241,300 cycles, whereas for a

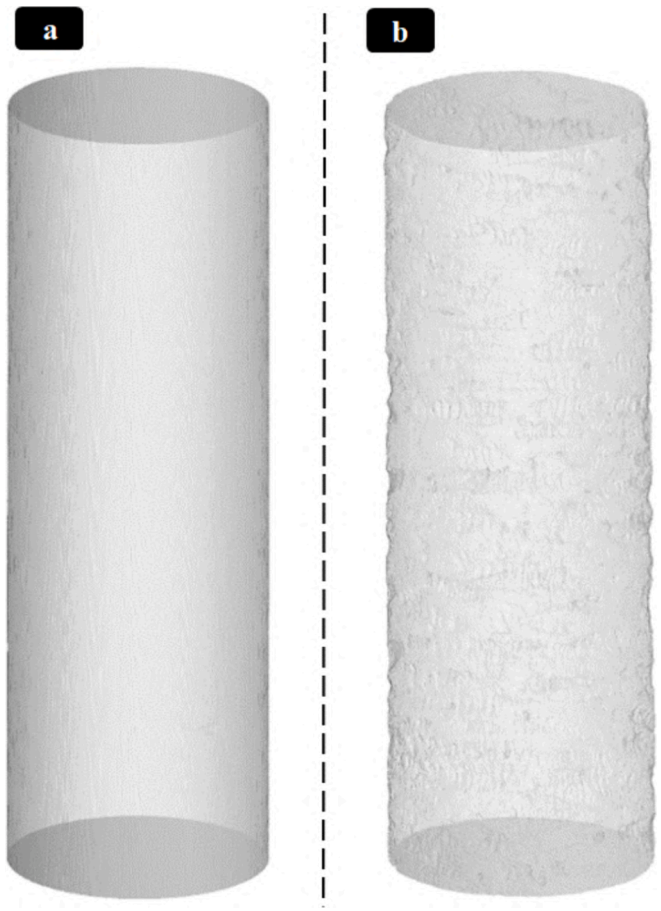


**Fig. 11.** Reconstructed volumes of a) SS316 non-corroded and b) SS316 pre-corroded.

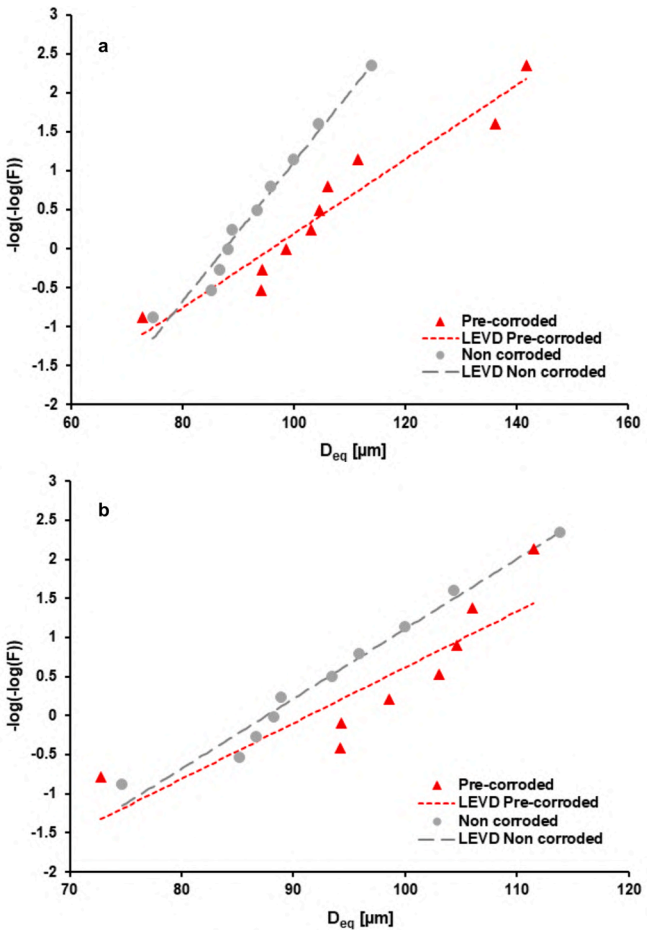


**Fig. 12.** Analysis of the internal defects carried out starting from micro-CT inspection a) defects on the Gumbel plot and estimated LEVDs b) defects on the Gumbel plot and estimated LEVDs, obtained by removing the largest and rare defects in the Pre-Corroded specimens.

pre-corroded specimen subjected to the same stress level, it was 45,400 cycles. This substantial reduction underscores the pronounced effect of corrosion on fatigue life under lower-stress conditions. Within the stress range of 325 to 275 MPa, the average decrease in lifetime percentage from non-corroded to pre-corroded specimens was 75 %, with some instances exceeding 80 %. For instance, at a stress level of 275 MPa, the non-corroded specimen exhibited an average of 826,360 cycles, while the pre-corroded specimen endured only 158,730 cycles. Within the last stress range of 275–203 MPa, data scattering decreased, the average lifetime from non-corroded to pre-corroded decreased by 53 %, and the fatigue limit difference between these two types of specimens was 17.1 %.

The results of the most comprehensive analysis of the experimental data using the ANOVA method are presented in Table 3. By employing the general factorial design method on two factors (corrosion and stress) with varying levels of each factor (ten levels for stress and two levels for corrosion), the design has demonstrated a model with a significant F-value. The influence of the stress amplitude on the fatigue life is expected: however, the stress amplitude has been considered as a factor to investigate possible interactions, i.e., a variation of the corrosion effect dependent on the used stress amplitude. Indeed, the influence of interactions is clear by considering the results of the ANOVA analysis in Table 3, with the p-value close to 0. Moreover, as expected also from Fig. 15 and by considering the residual normal plot in Fig. 16(a), corrosion has a substantial impact on the distribution of S-N data. The normal plot of residuals in the one-factor (stress) design was perfectly aligned with the red line (Fig. 16(a)). However, a slight distortion in the plot occurred due to the categorical factor of corrosion. Despite this, the model remains statistically significant, as indicated by the R-square value of 97.13 %. The accuracy of the model is also demonstrated by the predicted versus actual graph in Fig. 16(b), which demonstrates that the predicted data is 93 % accurate when compared to the actual data. As a result, the coded model format for the relationship between stress levels and categorical corrosion factors has been presented in Table 3. This model encompasses the S-N data from both pre-corroded and non-corroded experiments.

To explain this model, it is important to specify that it combined all non-corroded and pre-corroded data, with the impact of corrosion being evaluated as a categorical factor denoted by a coded value of 0 for non-corroded specimens and 1 for pre-corroded specimens. The model and residual data distribution of this model indicate a highly significant correlation between corrosion and stress. Based on the model's F-value, it appears that both variations in stress levels and specimen surface quality (pre-corroded or non-corroded) have a substantial and statistically significant impact. Furthermore, the effect of specimen surface quality (which has been considered as a corrosion factor in modeling) appears to be considerably larger. According to the results of the ANOVA study, corrosion phenomena have a slightly stronger influence on fatigue properties relative to alterations in stress level which means there is a significant relationship between corrosion and stress level effects on fatigue lifetime.

### 3.5. Fractography

#### 3.5.1. Entire fracture surface

To investigate fractography and determine the impact of stress level

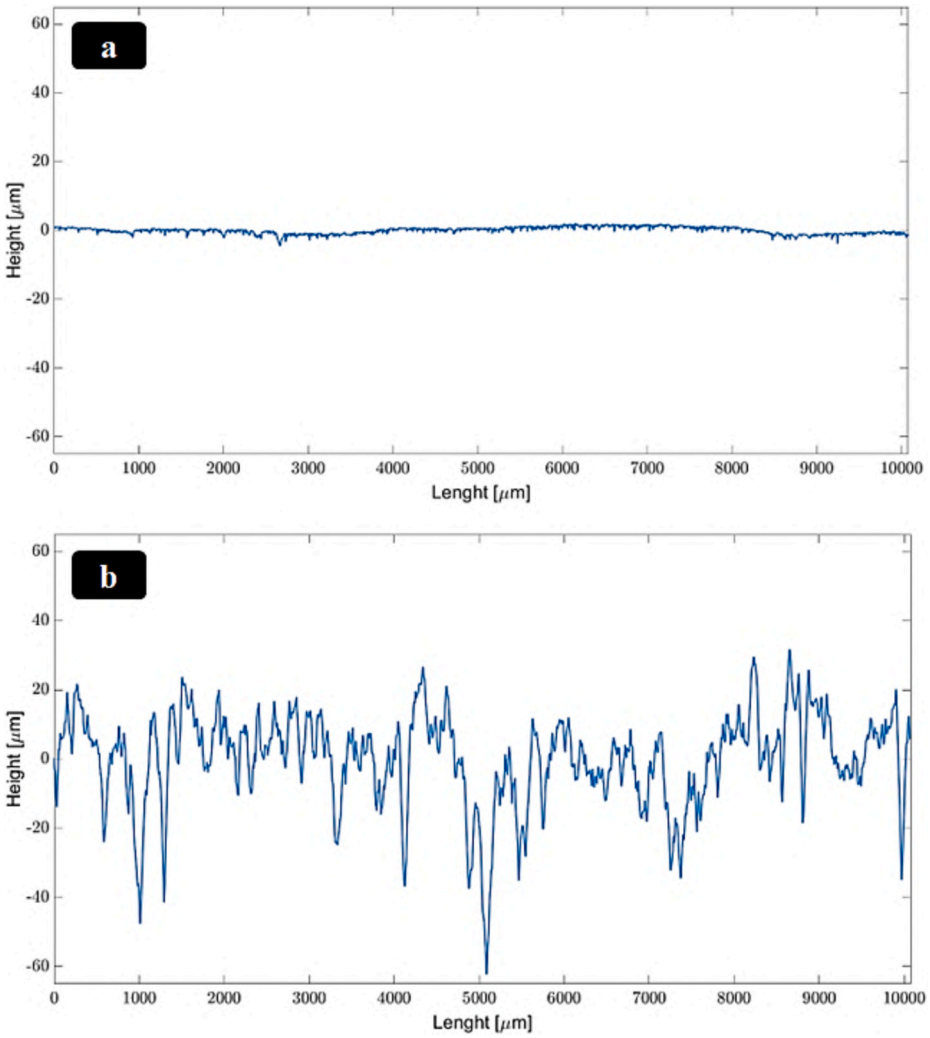


**Fig. 13.** Surface profile of a) non-corroded sample and b) pre-corroded sample.

**Table 2**
Roughness parameters of pre-corroded and non-corroded specimens, extracted by profilometry.

| Specimen | Ra [μm] | Rp [μm] | Rv [μm] | Rt [μm] |
|---|---|---|---|---|
| Non-corroded | 0.31 | 0.72 | 1.79 | 4.27 |
| Pre corroded | 7.18 | 16.70 | 25.20 | 60.80 |

The extracted parameters are following ISO 4287 standards:
Ra: Arithmetic average height of the profile.
Rp: Maximum peak height of the profile, expressed as the mean value over five sampling lengths.
Rv: Maximum valley depth of the profile, expressed as the mean value over five sampling lengths.
Rt: Maximum height of the profile between the highest peak and the deepest valley, expressed as the mean value over five sampling lengths.

and corrosion phenomena on the fracture surface and crack initiation, SEM and EDS were utilized to analyze fracture surfaces under two levels of elevated stress: 86 % of yield stress (420 MPa) and 56 % of yield stress (225 MPa). The results indicate that all crack initiation occurred at the surface. In the high-stress level test, the fractured surface exhibited a nearly equivalent area of propagation regime and ultimate fracture. Specifically, around 40 % of the fractured surface was occupied by the final brittle fracture, which was observed in both non-corroded and pre-corroded specimens. The fractured surface SEM images of non-corroded and pre-corroded specimens subjected to a stress level of 420 MPa are illustrated in Fig. 17. The crack initiation site is more evident in Fig. 17 (a) compared to Fig. 17(c). This discrepancy may be attributed to the fact that the non-corroded specimen has a distinct crack initiation site, whereas the local pitting on the surface of the pre-corroded specimen would facilitate multiple crack initiations.

In contrast to the divergent pattern observed in the pre-corroded specimen, the crack propagation regime (zone 1 in both images) exhibits a convergence pattern in the non-corroded specimen, resembling a white river or crack striation. Similar results were observed as the stress level decreased, even though the crack propagation zone was considerably larger in specimens subjected to high levels of stress. This observation provides evidence for the impact of surface pitting on crack initiation sites, thus, as the level of stress decreases, the impact of crack initiation becomes more significant, and the quality of the surface involved in crack initiation is critical. Specifically, it indicates that the white river marks in the pre-corroded specimen do not converge to a single point, suggesting that the material likely underwent multiple crack initiation sites. SEM examination of the fractured surface of a non-corroded specimen under a stress level of 275 MPa, as illustrated in Fig. 17(b), outlines that approximately 80 % of the crack propagation area exhibits smooth features, with striations converging towards the point of crack initiation. Conversely, in Fig. 17(d), the surface of the pre-corroded specimen exhibits parallel striations that closely resemble the brittle fracture pattern. Fig. 17(e) & (f) depict the schematic representation of the fractured surface pattern observed on each broken specimen. As documented in the literature [1,3,4,10,71], the convergent

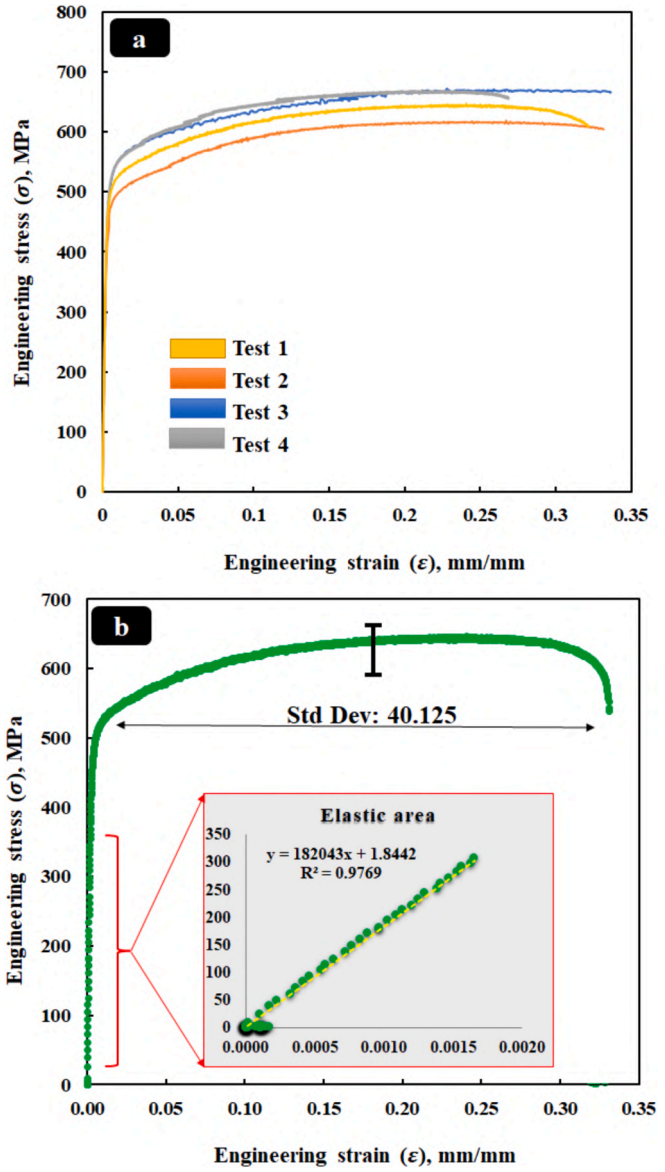


**Fig. 14.** a) Flow curves of four tensile tests, b) the average flow curve.

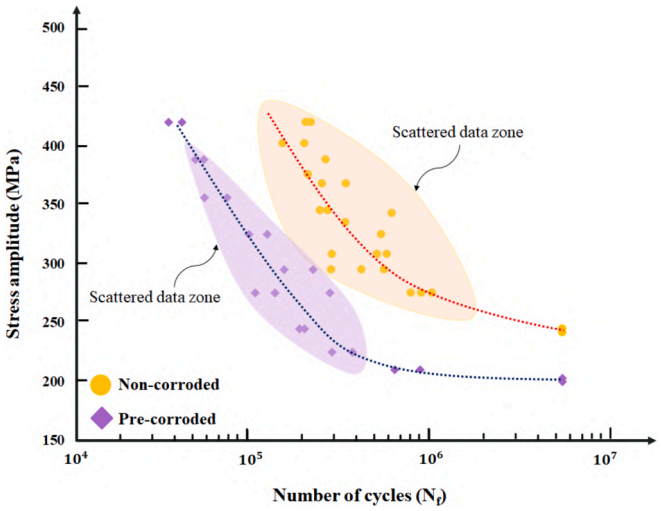


**Fig. 15.** S-N data for the non-corroded (virgin) and pre-corroded specimens with the scattered data zone.

marks pattern leading to the sites of crack initiation (surface defects) has been observed in non-corroded specimens (Fig. 17(e)). The pre-corroded specimen exhibits a nearly non-convergent pattern, which may be qualified to possible reasons; firstly, the presence of multiple crack initiation sites, expected to originate from surface pits; secondly, the observed brittleness of the material, which is surprising considering its composition as SS 316L with a yield point of 490 MPa; and thirdly, it is unlikely that hydrogen embrittlement significantly augmented the material's brittleness over the 10-day corrosion period. Hence, the nearly parallel marks observed in Fig. 17(f) can be attributed to the presence of numerous crack initiation sites on the surface, which rapidly interconnected the microcracks in the material.

### 3.5.2. Crack initiation

Fig. 18 illustrates the increased magnification of SEM images for the non-corroded specimen exposed to a stress amplitude of 420 MPa. As the magnification of images (a) through (f), the characteristics of fracture initiation become more apparent. The crack tip striation (white arrow in Fig. 18(d)) is more visible about the crack initiation zone; they indicate the cyclic opening-closing behavior of the crack point during the fatigue test. Upon closer examination approaching the initiation site, certain micro-ratchet marks extending perpendicular to the crack tip striations become discernible, as highlighted by the red arrows in Fig. 18(d). As one approaches the surface further, an additional mark emerges, resembling a folding-like extreme plastic local deformation that is thought to be a micro-chevron mark under bending stress conditions (green arrow). In this study, this chevron pattern was observed even at the macroscale on the most fractured surface of non-corroded specimens; this is consistent with what Hazra et al. [72], Alam et al. [73], and Padasale et al. [74] reported under bending fatigue conditions. The dimensions of the crack initiation defect were determined through the utilization of image processing analysis, the maximal length of the defect is 100.65 $\mu m$, while its depth is 38.82 $\mu m$. Given that the specimens have undergone machining, it is highly probable that the identified defect is porosity, which is consistent with the CT-scan images (Figs. 9 and 10). The CT scan analysis revealed that the largest porosities primarily formed in the surface layer of printed parts, specifically within a thickness of 1000 μm from the surface. Consequently, the presence of large porosities in the surface layer is more likely, as illustrated in Fig. 19. This finding verifies that the crack initiation site shown in Fig. 18 is a surface layer porosity situated on the free surface after machining. These defects were originally internal but became exposed on the surface following machining.

The crack initiation in a specimen that had been pre-corroded is depicted in Fig. 20 at various magnifications using SEM images. As previously stated, the crack's initiation site in these specimens is not a single point; rather, there appear to be multiple crack initiation sites on the surface, as illustrated in Fig. 20(a) & (b). A closer examination of one of these potential initiation sites would demonstrate the critical importance of the surface pits (Fig. 20(c) & (d)). A multitude of microcracks can be formed on the surface due to the network pattern of pits produced by the corroded surface (see Fig. 7(c) & (d)). Under cyclic loading conditions, these pits could potentially act as initiation locations for cracks to propagate in two directions: firstly, parallel to the stress gradient originating from the specimen's surface and passing through the neutral central axis, and secondly, perpendicular to the stress gradient in the width of the pit. As depicted in Fig. 20(d), crack propagation from pits can be categorized into two directions: one along the depth of the pit, and the other along the width of the pit, identical to the phenomena documented by Wang et al. [75], Tello et al. [76], and Almarez et al. [77], as well as the authors of another corrosion-fatigue study who proposed the same mechanism [2].

### 3.5.3. Crack propagation

The crack propagation area depicted in Fig. 21 illustrates the white

**Table 3**
Analysis of variance (ANOVA).

| Source | Sum of Squares | Degree of Freedom | Mean Square | F-Value | P-Value, Prob. > F |
|---|---|---|---|---|---|
| Model | 694.44 | 17 | 40.85 | 83.63 | <0.0001 |
| A-Stress | 533.46 | 9 | 59.27 | 121.35 | <0.0001 |
| B-Corrosion | 96.20 | 1 | 96.20 | 196.95 | <0.0001 |
| AB | 64.58 | 7 | 9.23 | 18.89 | <0.0001 |
| Pure Error | 20.51 | 42 | 0.49 | | |
| Cor Total | 714.95 | 59 | | | |
| **Std. Dev** | **0.70** | **R-Squared** | | **0.9713** | |
| **Mean** | **−2.28** | **Adj. R-Squared** | | **0.9597** | |
| **C.V.%** | **30.66** | **Pred. R-Squared** | | **0.9354** | |
| **PRESS** | **46.16** | **Adeq. Precision** | | **31.295** | |

A is the stress level and B is the coded effect of corrosion.
B: the coded format of corrosion phenomena which is defined as zero for non-corroded and one for pre-corroded.
R-squared: a statistical measure that represents the proportion of the variance for a dependent variable that is explained by an independent variable.
Adj R-Squared: an adjusted variant of R-squared, accounting for the number of predictors included in the model.
Adequate Precision: a signal-to-noise ratio. It contrasts the extent of predicted values dispersion at designated points with the typical prediction discrepancy.

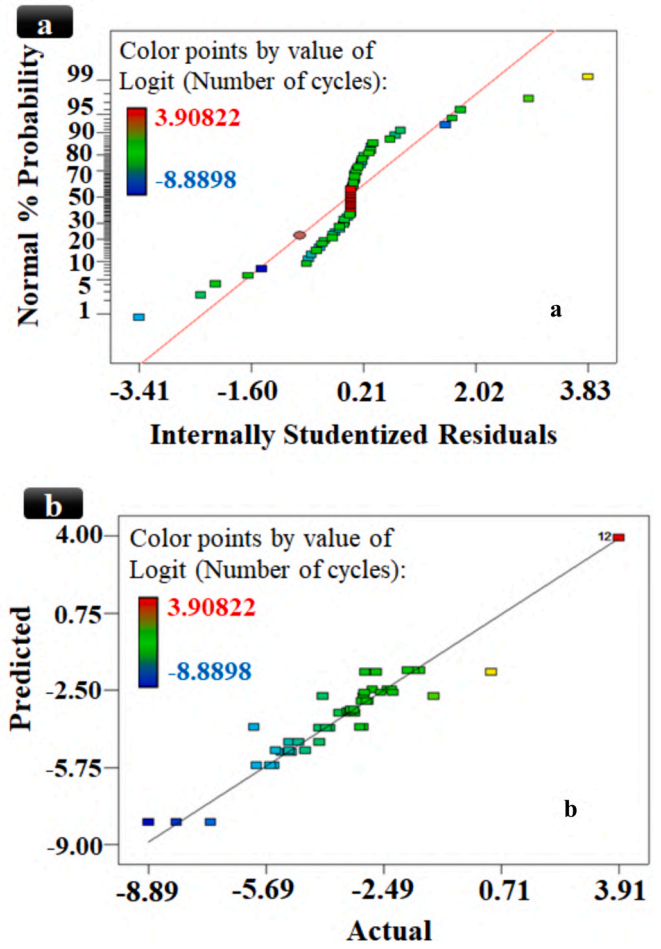


**Fig. 16.** The statistically analyzed data from the ANOVA method are used to estimate the precision of the model and experimental data; a) The normal plot of residuals; b) The comparison of predicted data from the ANOVA model with actual experimental data.

river pattern on the surface of the fractured specimen of Fig. 17. Some secondary microcracks can be observed in this region in the pre-corroded specimens. Upon comparing the fracture surfaces of the non-corroded specimen (Fig. 21(a)) and the pre-corroded specimen (Fig. 21(b)), it is evident that the pre-corroded specimen exhibits a greater portion of white rivers, indicating a more brittle mode of fracture, and has even witnessed the initiation of secondary cracks during crack propagation. At a higher magnification, certain defects are visible in Fig. 21(d), including striations marks of crack propagation and a discernible change in crack direction. These imperfections appear to be the result of inadequate fusion during the AM process and resemble a secondary crack initiation point, or crack switching mode. As can be observed in Fig. 21(f), the crack tip striation marks near these defects exhibit varying orientations, even though they traverse the interior surface of the defect.

The fracture surface of pre-corroded specimens exhibits signs of increased brittleness, potentially attributable to hydrogen embrittlement, which renders the surface more brittle than that of non-corroded specimens. The presence of secondary microcracks in the pre-corroded specimen may be attributed to this hydrogen embrittlement. While secondary microcracks are also evident in Fig. 21(e) of the non-corroded specimen, their quantity and sizes exhibit differences compared to those observed in the pre-corroded specimen. Additionally, a precipitate or inclusion in Fig. 21(e) appears as an internal defect inconsistent with the base material. Furthermore, it seems that the SIF surrounding the defect initiated some extremely small microcracks. EDS analysis of pre-corroded specimens revealed the presence of a small quantity of chlorine, as opposed to non-corroded specimens. The specimen is exhibiting embrittlement due to the penetration of $Cl^-$ [78] during a 10-day corrosion period under extremely aggressive $H^+$ and $Cl^-$ conditions. Throughout the ten days of corrosion, $Cl^-$ and $H^+$ reacted with the surface and certain elements on the surface, such as Mn (which has been identified as the primary anodic dissolution element in corrosive media [2,79]). Since the EDS results of the interior sections of the specimens indicate that there is approximately 0.1 % Cl, the diffused $H^+$ and $Cl^-$ are likely to be substantial.

The EDS and nano-indentation results of non-corroded and pre-corroded specimens (420 MPa stress level) are displayed in Fig. 22. The chemical analysis of the fractured surface in the crack initiation area reveals the presence of $Cl^-$ in the pre-corroded specimen, suggesting ionic diffusion and corrosion product precipitates, as shown in Fig. 22(a) and (b). The EDS map analysis of certain specimens revealed a variation in the $Cl^-$ percentage, despite all specimens undergoing the same corrosion procedure. Two pre-corroded samples are depicted in the EDS map concerning the $Cl^-$ element, showing a $Cl^-$ percentage ranging from 0.1 % to 1.4 % in Fig. 22(e) and (f). This research did not investigate the cause of this discrepancy; however, it appears that the stress amplitude and fatigue life are likely associated with the amount of $Cl^-$ remaining on the fractured surface. The primary findings of these EDS maps highlight the effect of $Cl^-$ as a potential corrosion product element on the surface (crack initiation site) and the diffusion of $Cl^-$, and likely H+, into the material. These findings necessitate further investigation in the future.

Fig. 22(c) and (d) present the nano-indentation results focusing on Young's modulus and hardness gradient in non-corroded and pre-

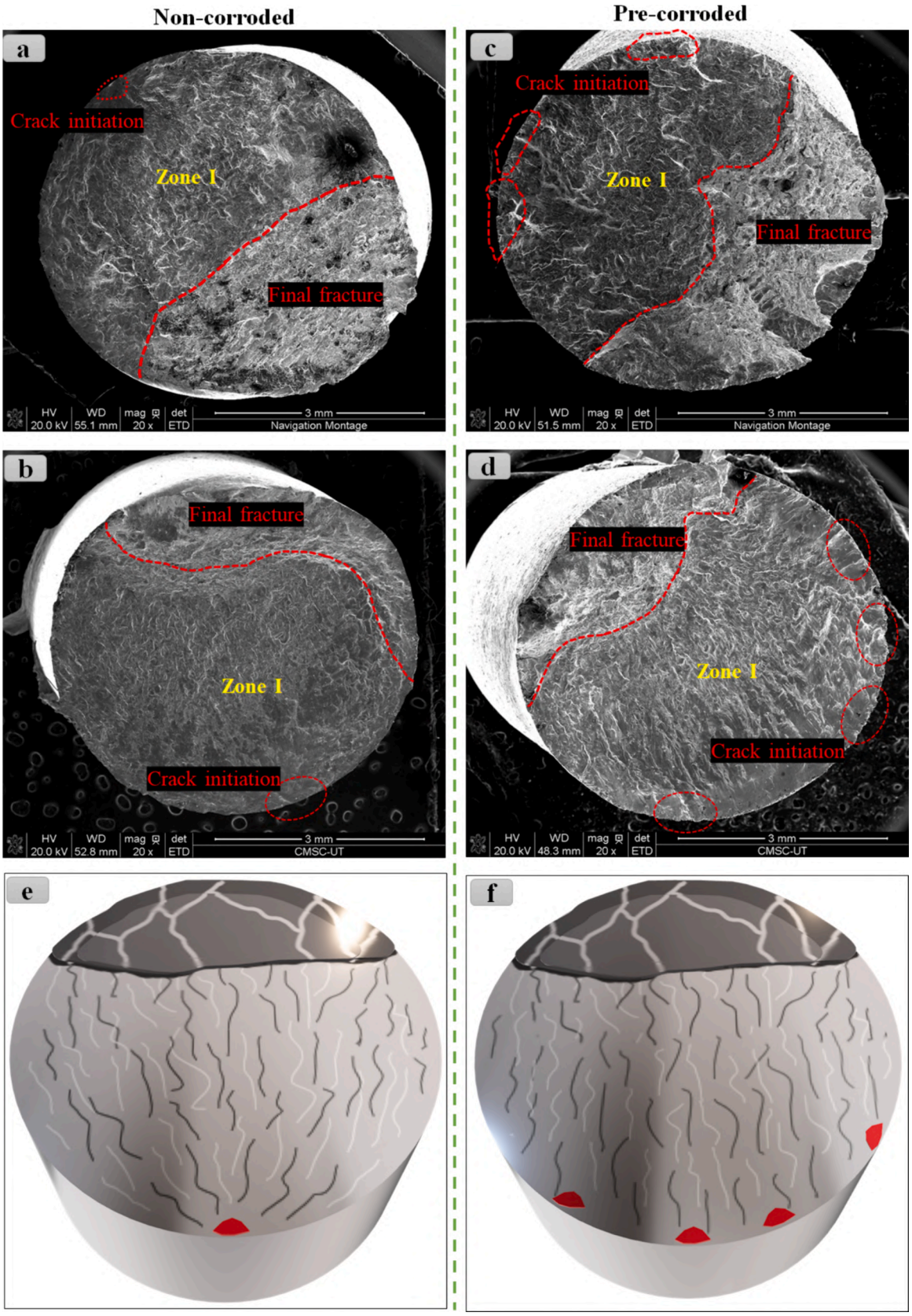


**Fig. 17.** SEM-based fractography of non-corroded specimens (a) 420 MPa stress level and (b) 275 MPa stress level, and pre-corroded specimens (c) 420 MPa stress level and (d) 275 MPa stress level. (e) and (f) the schematic of fractured surface striation pattern behavior in both non-corroded and pre-corroded specimens.

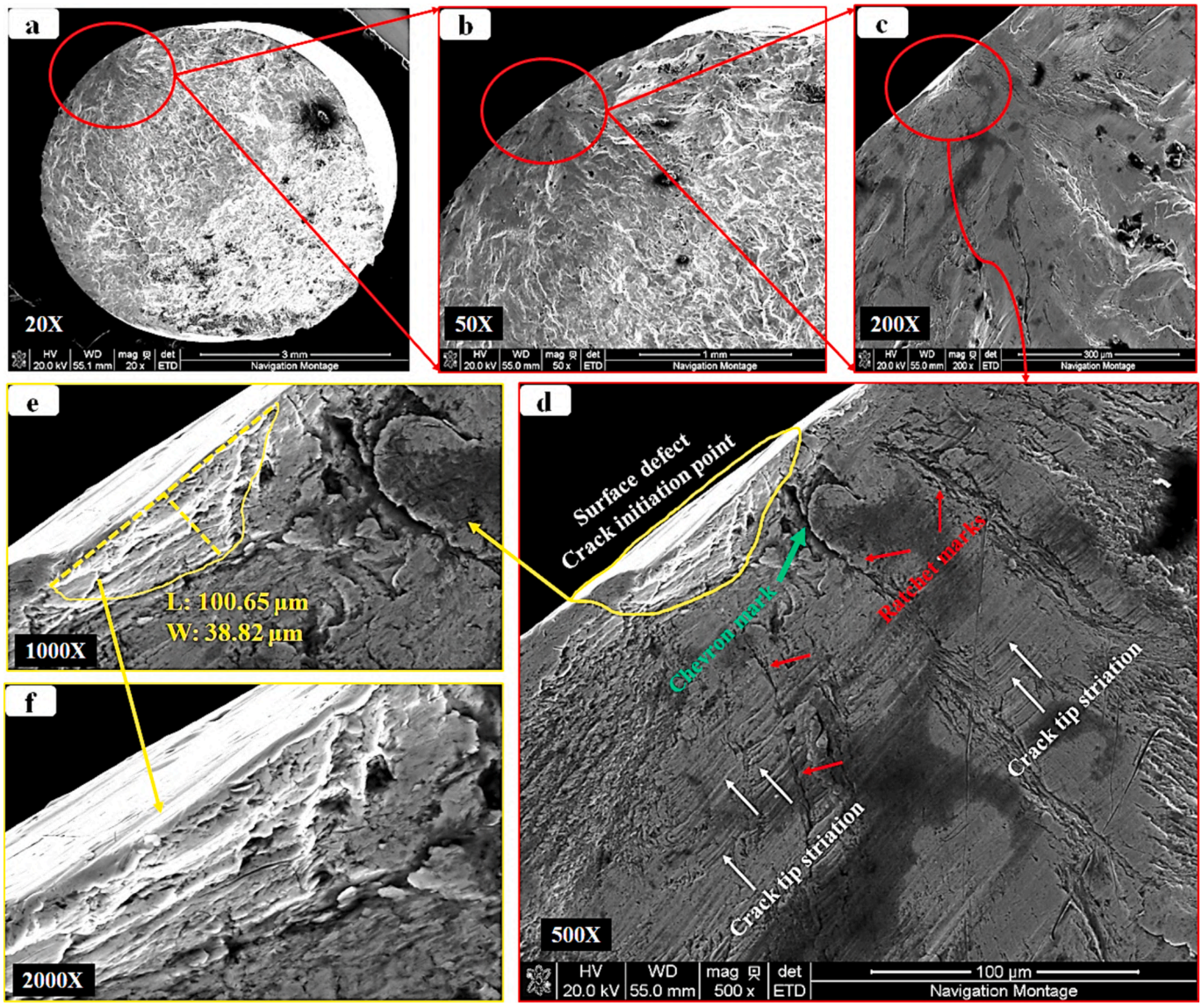


**Fig. 18.** SEM micrographs of the fractured surface of a non-corroded specimen; a) the entire fractured surface; b) the area of crack initiation and crack tip striation; c) the crack initiation area; d) the crack initiation area with marks denoted by white arrows; ratchet marks by red arrows; and a green arrow for the chevron mark; and e and f) a higher magnification of the defect located at the crack initiation point.

corroded specimens, particularly near the fractured surface. The hardness spreading of the two specimens appears to be quite similar; the averages of middle line hardness in Fig. 22(c) and (d) for the non-corroded and pre-corroded specimens were 241.2 HV and 233.3 HV, respectively. However, the noteworthy variance in hardness between the two specimens indicated by the nano-indentation close to the fractured surface provides evidence of small-scale plastic deformation beneath the fractured surface and likely dislocation accumulation.

The neutral axis, which comprises the middle of these specimens, is not anticipated to experience substantial work hardening. Therefore, the average of the middle line hardnesses has been regarded as indicative of specimens with hardnesses that are relatively close to one another. Nevertheless, the stress distribution would have been different during the propagation period due to crack propagation. Upon examining the IAMA and KAM images in Fig. 23, we are unable to confirm the presence of substantial work hardening in the middle line of specimens. Additionally, we did not anticipate that corrosion would affect the middle line hardness. Hydrogen embrittlement, which alters the material's hardness properties, is thus the only factor that could affect the middle line hardness of corroded specimens; however, since no significant differences in middle line hardness were observed between non-corroded and pre-corroded specimens, we cannot consider that corrosion affects the middle line hardness of the material (far from the surface).

The data in Fig. 22(c) indicates that the hardness values beneath the fractured surface differ significantly from the average hardness values along the middle line. The average hardness values for the top left and right measurements (triangle symbols in Fig. 22(c)) are 327.9 HV and 366.3 HV, respectively, with a maximum hardness of 381.7 HV and 342.5 HV for the top right and top left, and 326.7 HV for the top middle line, which is directly beneath the fractured surface along the neutral axis of the specimen. On pre-corroded specimens, nearly identical behavior was observed; however, the hardness values varied. The average hardness values were 335.3 HV and 237.5 HV, respectively, in the upper left and right corners, and 233.3 HV along the middle line. The hardness values observed in the thin fracture layer deviated slightly from the average. Specifically, the highest hardness was recorded at 351.8 HV in the upper left corner, 245.9 HV in the upper right, and 275.6 HV in the middle.

The disparity observed between the two specimens cannot be solely

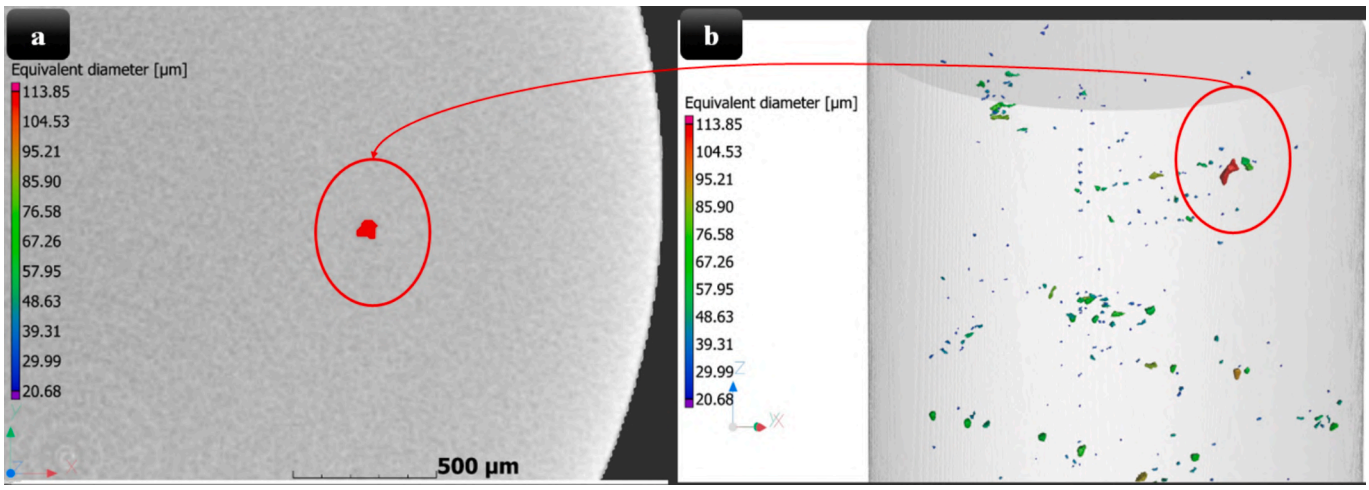


**Fig. 19.** The CT scan results indicate that the surface layer* contains the greatest size of porosity. *Note**.** The surface layer considered in this investigation was 1000 $\mu m$ in thickness before machining. As a result of machining removing this surface layer, defects emerged on the free surface.

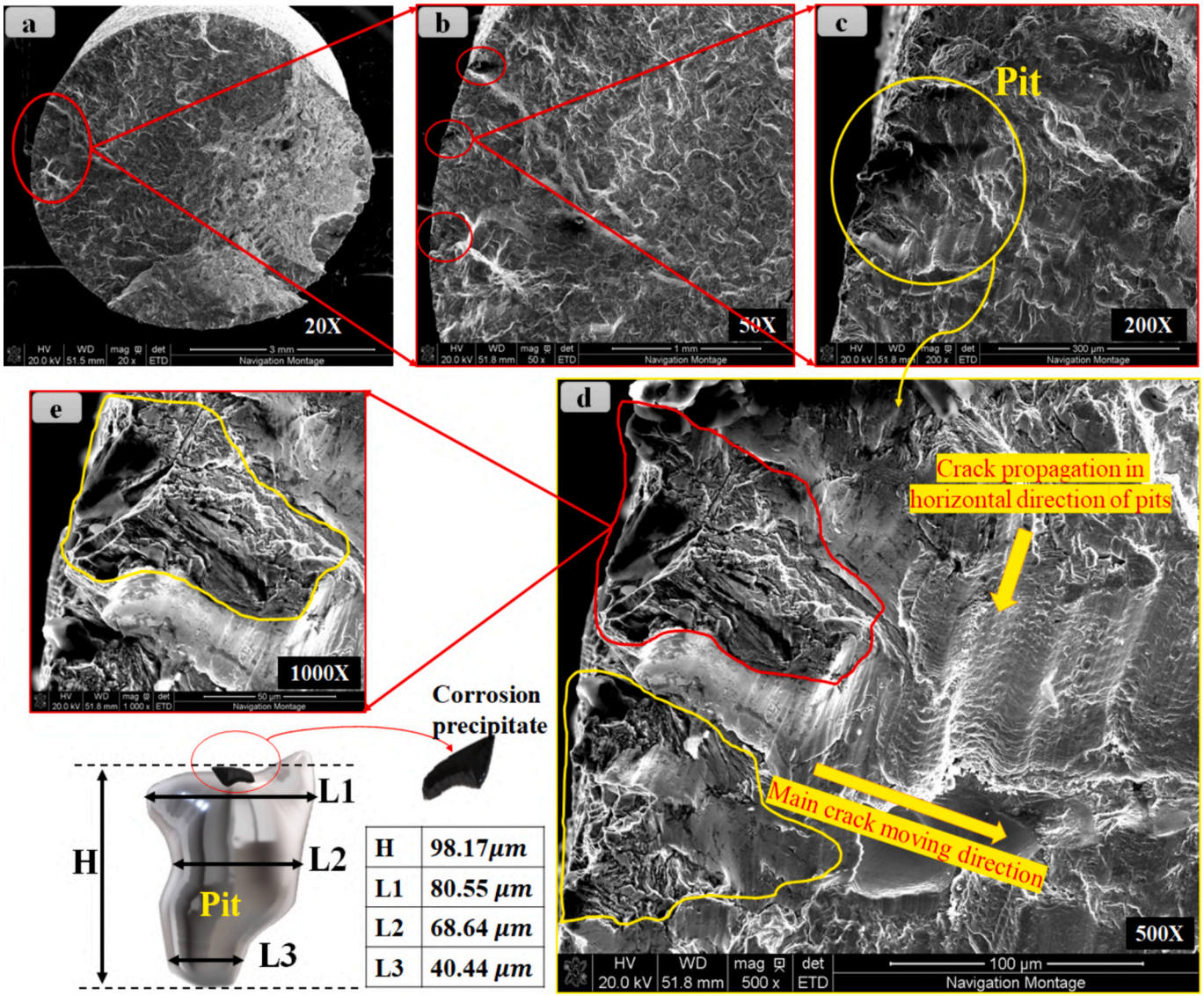


**Fig. 20.** SEM micrographs of the fractured surface of a pre-corroded specimen: a) the entire fractured surface; b) the area of crack initiations and striation; c) one of the crack initiation areas (likely corrosion pit); d) the crack initiation area with striation denoted by red and yellow curvatures; and e) a higher magnification of the pitting located at the crack initiation point with the schematic of pitting and dimensions.

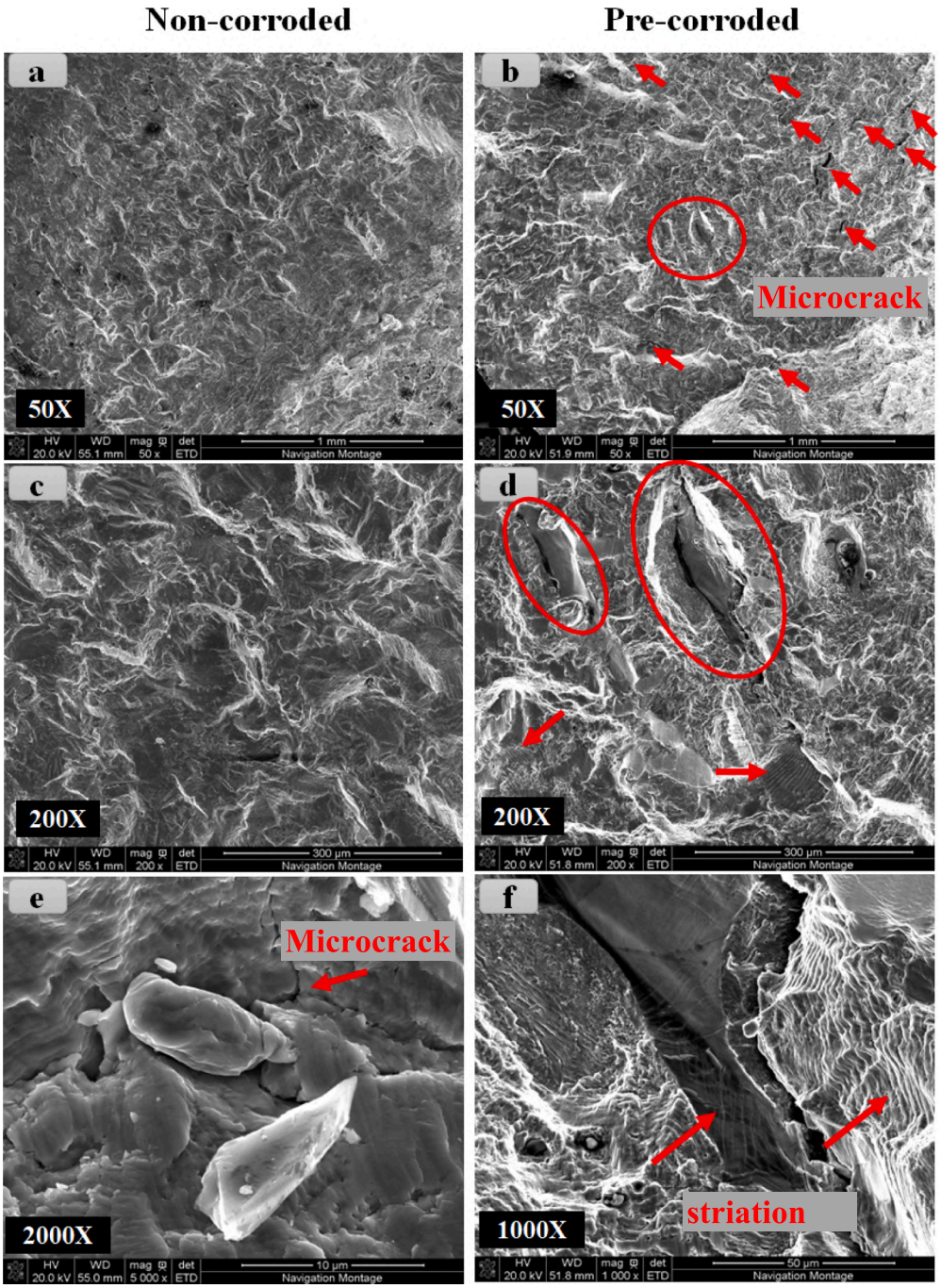


**Fig. 21.** The crack propagation area of the fractured surfaces of pre-corroded and non-corroded specimens is illustrated in a) to f). At various magnifications, the crack propagation area of the non-corroded specimen is seen in images a), c & e) with a minor secondary internal microcrack surrounding a defect in e). The crack's propagation area in the pre-corroded specimen is illustrated in images b), d), and f), which also feature secondary internal microcracks and a crack striation mark.

attributed to work hardening, as both were subjected to identical stress amplitudes (420 MPa) during testing, rendering it challenging to distinguish the root cause of the discrepancy. However, the sole distinguishing factor between these experiments is corrosion; yet we refrain from categorizing it as the primary cause. Substantiating the hypothesis that hydrogen embrittlement influences this behavior empirically poses challenges due to negligible fluctuations in average hardness along the neutral axis. The only information that can be provided is the difference in Young's modulus between the two specimens, which may indicate hydrogen embrittlement. Contrary to expectations, where work hardening was anticipated due to hydrogen embrittlement, an inverse trend is evident. Notably, discrepancies in hardness values are observed at the corners of both specimens, with one corner in each exhibiting notably lower hardness. Noteworthy is the observation that crack initiation and propagation originated from the same side in both specimens. Therefore, the propagation process endured a prolonged duration, resulting in one side experiencing heightened stress intensity, slip band movement, shear line phenomena, and work hardening compared to the other. Meanwhile, the opposing side, where the crack initiated, witnessed the greatest stress amplitude, thereby inducing a higher stress intensity factor and more localized plastic deformation. Consequently, the variance in corner hardness is attributed to crack propagation originating from one side.

The pre-corroded specimen exhibited a lower average Young's

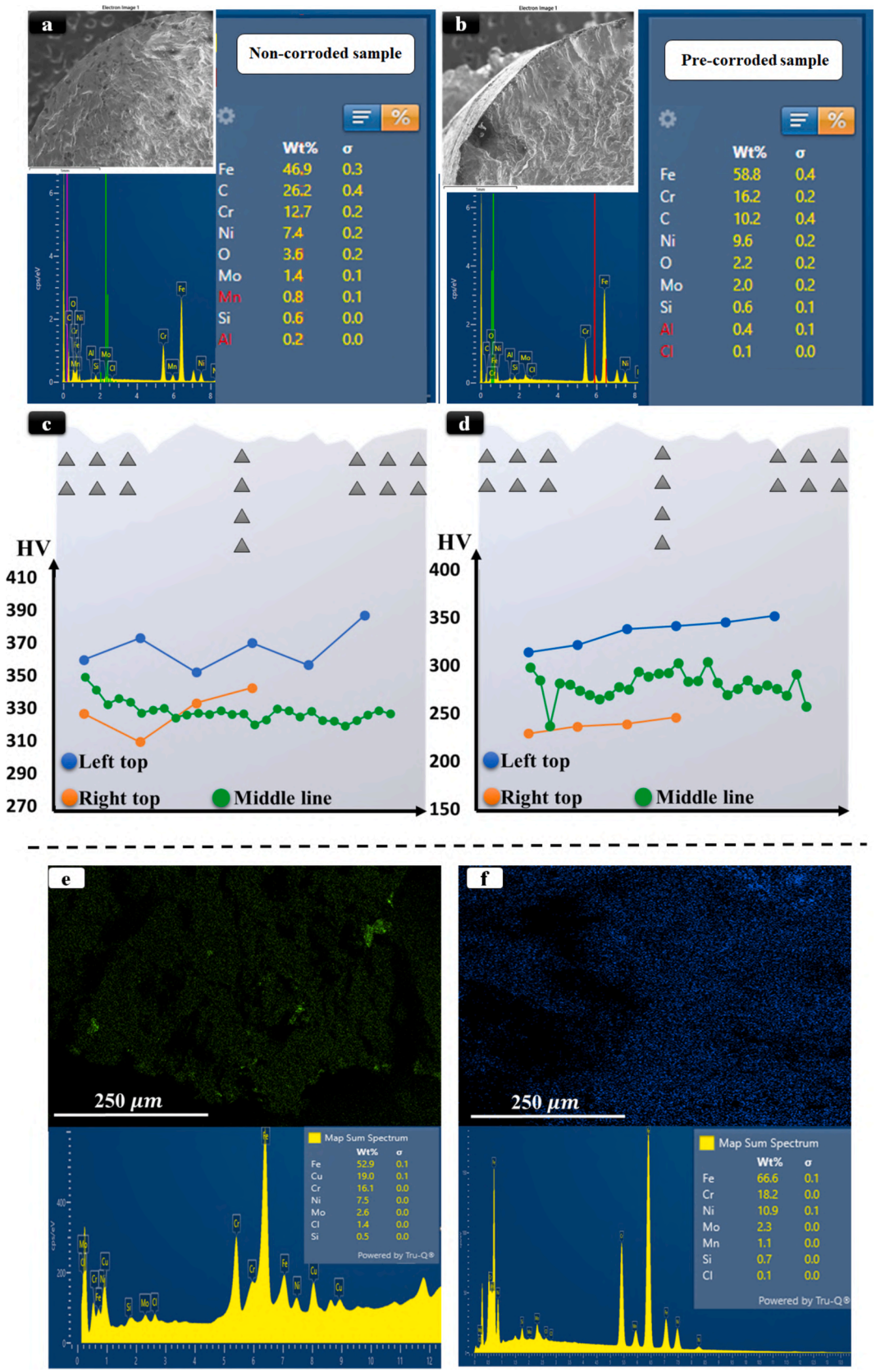


**Fig. 22.** The chemical composition of two specimens (420 MPa stress level), a) non-corroded and b) pre-corroded, is determined using EDS. The nano-indentation results for hardness and Young's modulus of both specimens are displayed in c) for non-corroded and d) for pre-corroded, e) EDS map result of pre-corroded specimen under 275 MPa and f) under 360 MPa.

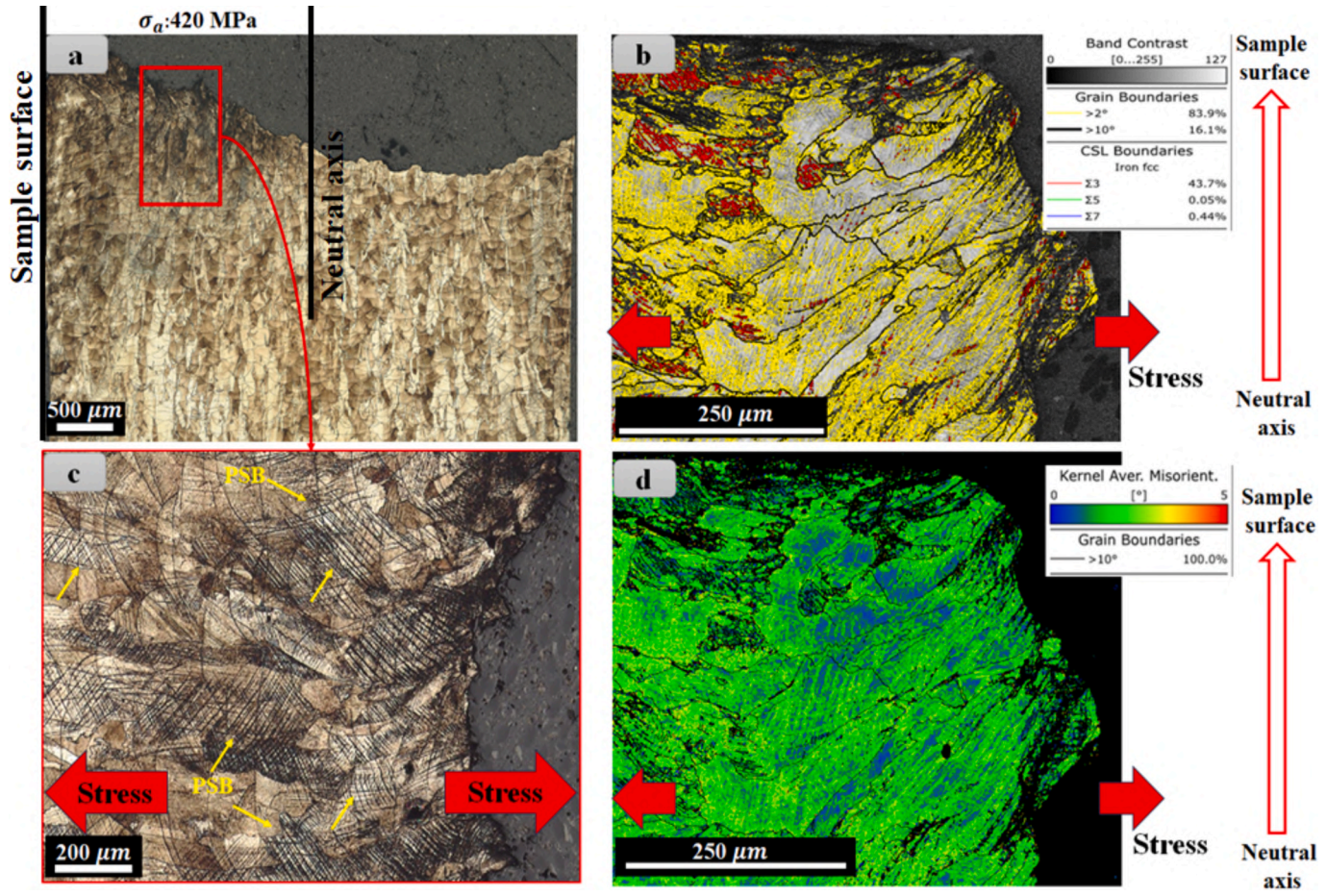


**Fig. 23.** a) OM image of the fractured surface cross-section of the non-corroded specimen under 420 MPa stress amplitude, in the higher magnification the dark black lines are showing slip lines close to the fractured surface, b) SEM-based EBSD images with internal average misorientation angles (IAMA) expression, c) is showing the higher magnification of fractured surface layer with slip lines, d) the kernel average misorientation (KAM) expression on EBSD image.

Modulus (E) than the non-corroded specimen: E = 170.6 GPa and 233.3 HV compared to E = 186.1 GPa and 241.2 HV for the non-corroded specimen. The discrepancy in Young's modulus could potentially be attributed to the effect of corrosion on the elastic properties of the material, rather than work-hardening, which is a plastic region property. Concerning this matter, Young's modulus values for the corners indicate; the left corner 162.1 GPa, the right corner 146.2 GPa, and the middle line 170.6 GPa. Given that the middle line of Young's modulus is regarded as the reference value (due to its location along the neutral axis and near-zero stress experience), any decrease in Young's modulus should be attributed to material composition changes in the vicinity of the surface. Such alterations could potentially result from corrosion.

The effect of stress level on the behavior of the fracture surface and microstructure did not exhibit significant differences between specimens subjected to corrosion and non-corroded ones, both have similar behavior. To study the effect of stress level on the microstructure of fractured layers, Figs. 23 and 24 present the EBSD and OM results corresponding to two stress values, 275 and 420 MPa, from fatigue tests conducted on non-corroded specimens. OM images of fracture surface perpendicular sections reveal melt pool layers and grains (see Fig. 23(a) and (c)). Dark black, angularly oriented, narrow lines at high magnification indicate the presence of slip lines in the microstructure, which are denser about the fracture surface. Analysis of the kernel average misorientation (KAM) and internal average misorientation angles (IAMA) expression images in Fig. 23(b) and (d) from the near-fractured surface layer reveals that the EBSD image exhibits a significant grain boundary percentage. The yellow lines in Fig. 23(b), which cover about 83.9 % of the grain boundaries, potentially represent slip lines (resulting from dislocations pile up) that are expected to accumulate and form persistent slip bands. Moreover, the high percentage of the $\sum 3$ (43.7 %) in Fig. 23(b) illustrates the possibility of the formation of twins which occurred during the deformation in this area [80]. The KAM factor depicted in Fig. 23(d), illustrating angles between 1–3 degrees across nearly all the cracked surface layers, indicates a misorientation of the microstructure in the preferred direction. Similar phenomena have been observed at lower stress amplitudes (275 MPa), albeit with a reduced intensity compared to higher stress levels. As shown in Fig. 24, the fractured surface perpendicular section OM picture exhibits lighter slip lines. Fig. 24(b) and (d) exhibit much lesser misorientation (local plasticity) than Fig. 23, which is predicted given the decreased stress amplitude. By comparing the results presented in both Figs. 23 and 24, it can be deduced that the stress level, characterized by the pronounced stress gradient from the specimen's surface to the neutral axis at its center, leads to enhanced local plasticity and increased activation of PSBs (persistent slip bands). Because of the non-constant stress distribution in the cross-section (Fig. 5(b)), a slight misorientation angle of 2–4 degrees between various layers of the cross-section has emerged. Therefore, in the RBF test, as predicted, the stress gradient and stress level had a substantial influence on PSB mobility and the local plasticity intensity adjacent to the fractured surface.

### 3.6. Modeling

In linear elastic fracture mechanics (LEFM), the SIF is frequently regarded as the primary force underlying the propagation of cracks. When $\Delta k$ is greater than $\Delta k_{th}$, the crack is said to be propagating. The

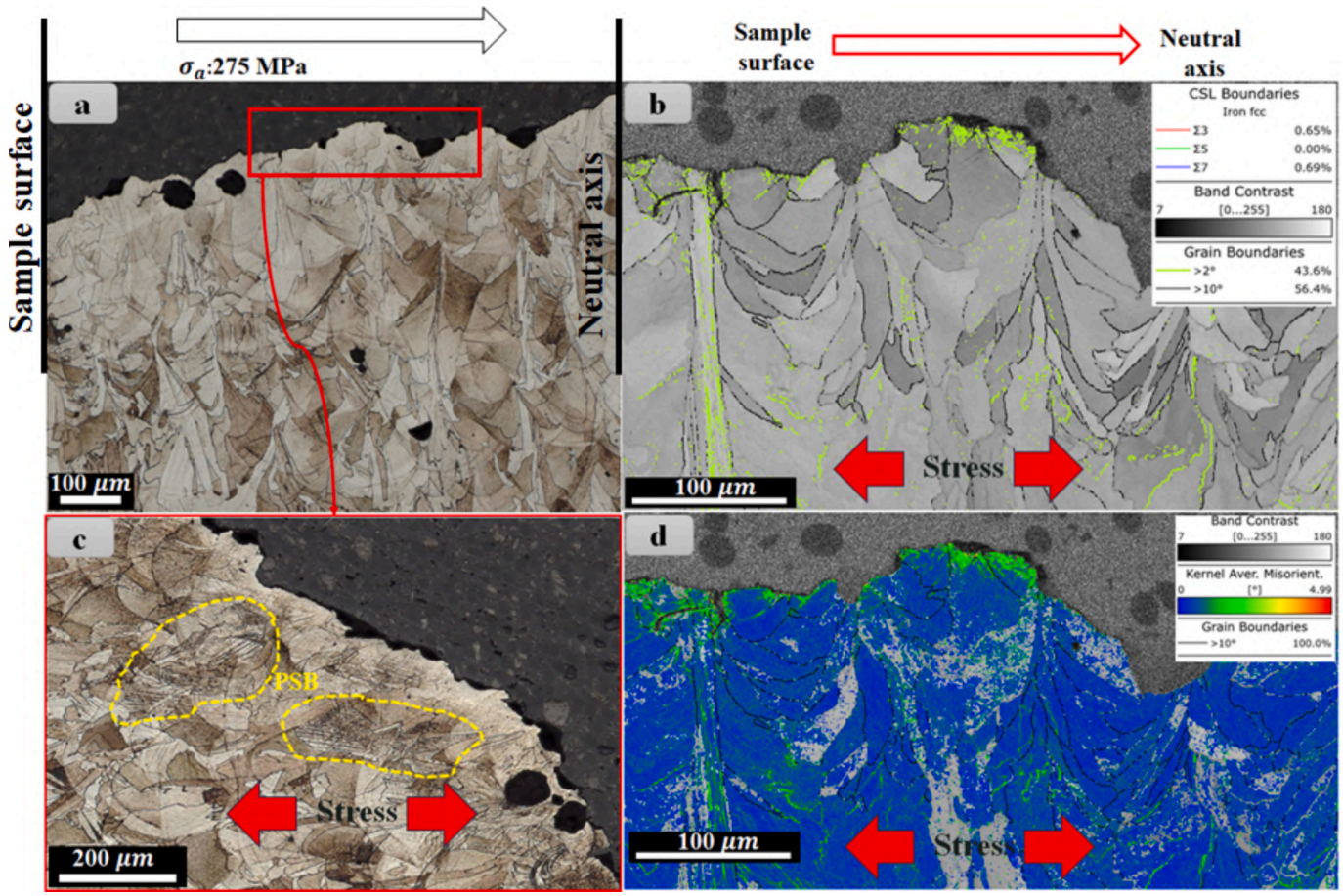


**Fig. 24.** a) OM image of fractured surface cross-section of the non-corroded specimen under 275 MPa stress amplitude, in the higher magnification the dark black lines are showing slip bands close to fractured surface, b) SEM-based EBSD images with internal average misorientation angles (IAMA) expression, c) is showing the higher magnification of fractured surface layer with slip bands, d) the kernel average misorientation (KAM) expression on EBSD image.

crack expansion size for long cracks may exhibit a direct correlation with the SIF by employing the Paris law [65,81]:

$$\frac{da}{dN} = A.\Delta k^{b} \tag{3}$$

By utilizing two material parameters, $a$ and $b$. Nevertheless, this expression becomes invalid when considering a short-crack propagating regime. One can locate a reformed form of the Paris law in the literature [82,83], which is utilized to characterize the behavior of both short and long cracks:

$$\frac{da}{dN} = C^{*}.(\Delta k - \Delta k_{th})^{m} \tag{4}$$

$C^{*}$ and m, are two material parameters equal to $6.25 \times 10^{-10}$ and 3.94, respectively, according to Merot et al. [15,70] and Riemer et al. studies [84]. Equation 8 incorporates the SIF threshold, and the crack propagating driving force is determined by the difference between $\Delta k$ and $\Delta k_{th}$. Short cracks have values of $\Delta k_{th}$ that are near $\Delta k$, resulting in a decelerated propagation rate. Given that $\Delta k_{th}$ is contingent upon $R$, considering the threshold also establishes a correlation between the applied stress ratio and the crack propagation behavior [85]. The fatigue life prediction in this research was conducted using Eq. (5) (Murakami's equation [64]).

$$\Delta k_{th} = g(HV + 120)a^{\frac{2}{n}}(\frac{1-R}{2})^{\alpha} \tag{5}$$

where $g = 3.3 \times 10^{-3}$ and $2.77 \times 10^{-3}$, for external and internal cracks respectively, $HV$ is the Vickers hardness, $a = \sqrt{area}$ is the crack length (or defect projected length) in $\mu m$, $R$ is the stress ratio, $n$ is an exponent in the original Murakami's model, and $\alpha = 0.226 + HV \times 10^{-4}$. Given the semi-experimental concept behind Murakami's model, it is conceivable that certain coefficients or exponents could be optimized following our experimental findings for AM'd SS 316.

The final crack length was determined using SEM data and Murakami's equation has been substituted in Eq. (5). The following equation is the resulting fatigue life prediction equation which has been utilized for generating the Fig. 25 diagram.

$$\frac{da}{dN} = C^{*}.(g(HV + 120))^{m}.(a^{2/n} - a_{in}^{2/n})^{m} \tag{6}$$

The constant parameters $n$, $m$, and $C^{*}$ have been previously specified, therefore, Eq. (6) would be simplified into Eq. (7):

$$N_f = \int_{a_{in}}^{a_f} \frac{40.568}{(a^{1/3} - a_{in}^{1/3})^{3.94}}.da \tag{7}$$

The final crack length could be estimated using SEM images by calculating the crack propagation area just before the final brittle fracture. The five SEM images and their corresponding final crack length estimations are displayed in Fig. 25(a). It seems that the fatigue life predicted by the model derived in Eq. (7) using the Paris law and Murakami's expression is nearly within the range of experimental data (Fig. 25(b), red triangles). The predicted data derived from the crack propagation modeling using Eq. (7) are presented in Fig. 25(b). The predicted data lies within the experimental regions (less than 10 % deviation) in this diagram. It is crucial to note that the modeling in this study does not account for the corrosion phenomena, as the corrosion

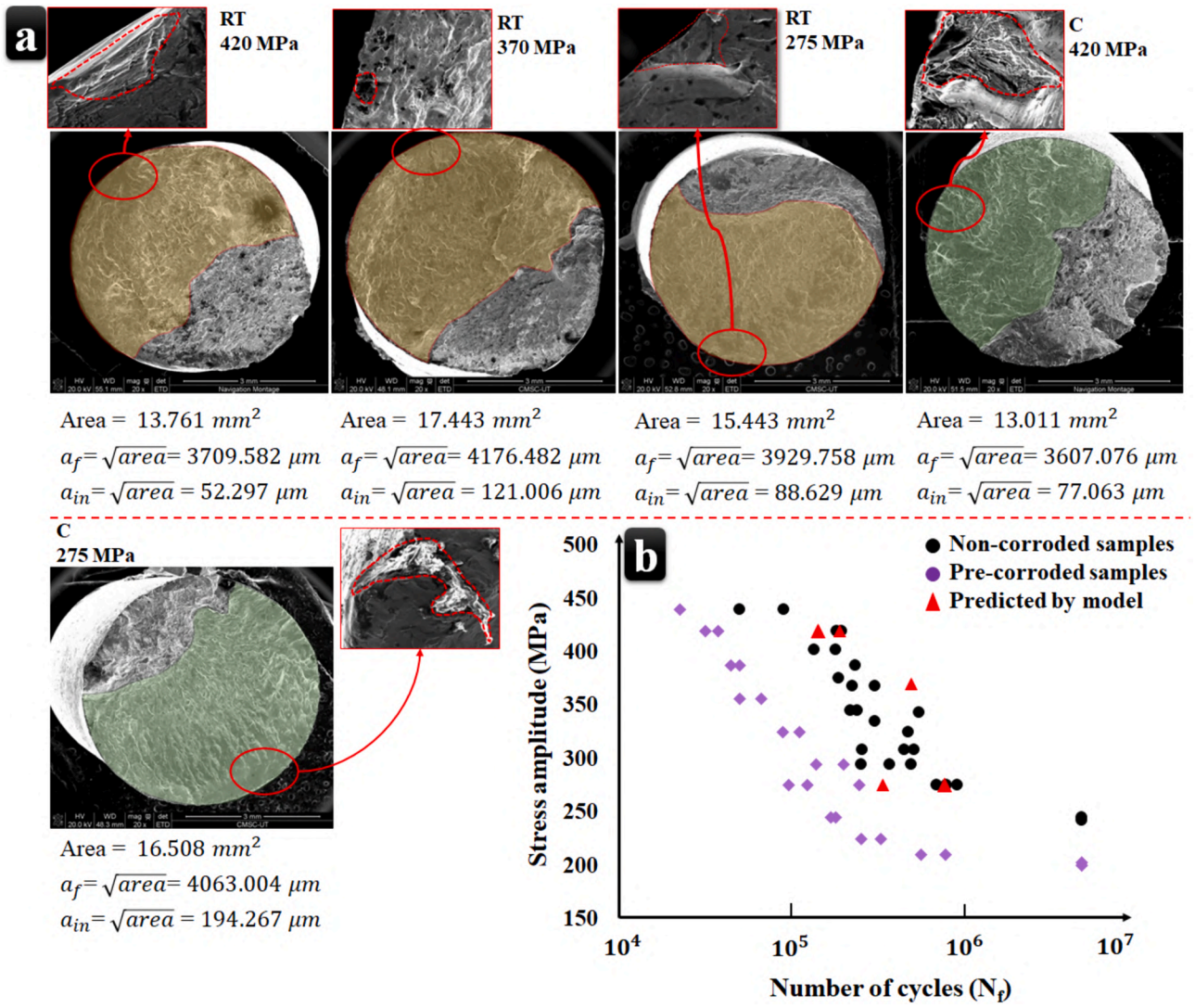


**Fig. 25.** a) the initial & final crack size measurement based on SEM images, (b) experimental and predicted data from Eq. (7).

effect is assumed to be a common surface defect. Consequently, the nature or type of the defect is not considered in the predictive model, which is based on the final crack length and defect size obtained from SEM results.

### 3.7. Ex-situ (relative to in-situ) corrosion RBF

The current ex-situ corrosion RBF research can be considered as a baseline for our future test setup to conduct in-situ corrosion RBF on AM'd SS316L. The application of *in-situ* corrosion RBF testing in comparison to *ex-situ* corrosion RBF testing of AM'd SS 316L presents an opportunity for fundamentally and comprehensively evaluating material performance under real-world service conditions. In-situ testing offers the advantage of simulating the actual operational environment more accurately, thereby providing insights into the combined effects of mechanical cyclic loading and corrosion exposure. This methodological approach facilitates a more robust assessment of material durability and reliability, particularly relevant in applications where structural integrity, exposed to surrounding aggressive environments, is dominant. Moreover, considering the potential impact of temperature and concentration variations of the corrosion solution on fatigue life is vital, as these factors can intricately interact with material properties and degradation mechanisms [86–88]. Temperature variations can influence corrosion rates and the kinetics of fatigue crack propagation, while alterations in solution concentration may affect corrosion kinetics and the formation of protective surface films. Understanding the interplay between these parameters is essential for accurately predicting the long-term performance of AM'd SS316L components in corrosive environments, thereby informing optimal design and material selection approaches.

## 4. Summary

Examining the RBCF characteristics of LPBF 316L stands as a pivotal endeavor for applications in marine, shipbuilding, naval, and naval aviation domains. Through RBF analysis, the material's response to the influences of cyclic loading and corrosive surroundings can be precisely evaluated (particularly the effect of corrosion-induced surface pitting considering that in the RBF test, the surface is exposed to the maximum stress distribution), essential for upholding structural robustness, longevity, and operational safety in maritime and naval contexts. In other words, RBCF enables meticulous study of surface alterations induced by mechanical strains and corrosive elements, providing important insights into the material's vulnerability to fatigue-driven failure and corrosion-induced deterioration in marine settings to meet the exacting demands of critical maritime and naval applications.

The results of this study, which is the first to quantify the corrosion-fatigue response of LPBF SS 316L in the RBF test, demonstrate the

significant influence of corrosion after ten days of immersion in corrosive conditions. Under ambient conditions, RBF tests were performed on both uncorroded and pre-corroded specimens. Following the microstructure investigation, mechanical characteristics such as tensile tests and nano-hardness measurements were assessed. The examination of the microstructure using SEM, and EBSD provides comprehensive insights into the influence of stress gradient and surface quality on the fatigue characteristics of AM'd SS316L alloy subjected to the RBF test.

The main findings of this research are as follows:

1. The pre-corroded specimen had an average 20 % lower fatigue strength than the non-corroded specimen. At lower stress levels (388 to 356 MPa), pre-corroded specimens showed a 70 % reduction in lifetime compared to non-corroded specimens. Within the 325 to 275 MPa stress range, the average lifetime decrease from non-corroded to pre-corroded specimens was 75 %, in some instances exceeding 80 %. At 275 MPa stress, non-corroded specimens endured 826,360 cycles, while pre-corroded specimens endured 158,730 cycles, showing a significant reduction. Within the 275–203 MPa stress range, the average lifetime decrease from non-corroded to pre-corroded was 53 %, with a 17.1 % difference in fatigue limit.
2. The fatigue limit for non-corroded and pre-corroded specimens, 242 and 203 MPa were demonstrated by the S-N data trend, together with a broad scatter between $10^5$ and $10^6$ cycles.
3. The pre-corroded specimen showed less dispersion, demonstrating the critical role that pitting plays in the onset of cracks.
4. According to the EBSD results, the fracture layer work-hardening and intensity of persistent slip lines were significantly influenced by the stress gradient and stress level, as demonstrated by the results of the nano-indentation hardness and fractography.
5. As stress levels decreased, the crack initiation role became more significant, emphasizing the critical role of surface quality.
6. The predicted data based on the developed model showed high accuracy (less than 10 % deviation) with the experimental data.

This study on RBF testing of AM'd SS316L conducted a comprehensive examination of surface-dependent phenomena, notably ex-situ corrosion in environmental conditions. While alternative fatigue tests such as multiaxial, ultrasonic, and uniaxial tests offer possibilities to explore in-situ and ex-situ corrosion-fatigue properties of AM'd metallic materials, prioritizing the elimination of internal defects is desirable when investigating the influence of surface conditions on fatigue behavior. Consequently, RBF emerges as a viable method for assessing the environmental impact on fatigue properties, by effectively controlling for internal defects and imposing a maximum stress gradient on the surface. Nonetheless, further investigation is warranted to explain the underlying mechanisms governing environmental effects, in-situ corrosion processes, the geometric and spatial distribution of pits, the influence of corrosive elements, and other relevant factors.

## CRediT authorship contribution statement

**Alireza Behvar:** Writing – original draft, Methodology, Investigation, Data curation. **Yahya Aghayar:** Writing – original draft, Investigation, Formal analysis, Data curation. **Maryam Avateffazeli:** Methodology, Data curation. **Andrea Tridello:** Writing – review & editing, Validation, Software, Formal analysis, Data curation. **Alessandro Benelli:** Software, Methodology. **Davide S. Paolino:** Writing – review & editing, Validation, Methodology, Investigation. **Mohsen Mohammadi:** Writing – review & editing, Resources, Project administration, Investigation. **Meysam Haghshenas:** Writing – review & editing, Supervision, Resources, Project administration, Conceptualization.

## Declaration of competing interest

The authors declare that they have no known competing financial interests or personal relationships that could have appeared to influence the work reported in this paper.

## Data availability

Data will be made available on request.

## References

[1] Stephens RI, Fatemi A, Stephens RR, Fuchs HO. Metal fatigue in engineering. John Wiley & Sons; 2000.
[2] Behvar A, Haghshenas M. A critical review on very high cycle corrosion fatigue: Mechanisms, methods, materials, and models. J Space Safety Eng 2023;10(3):284–323.
[3] Behvar A, Berto F, Haghshenas M. A review on isothermal rotating bending fatigue failure: Microstructural and lifetime modeling of wrought and additive manufactured alloys. Fatigue Fract Eng Mater Struct 2023;46(8):1–51.
[4] Shrestha R, Simsiriwong J, Shamsaei N. Fatigue behavior of additive manufactured 316L stainless steel under axial versus rotating-bending loading: Synergistic effects of stress gradient, surface roughness, and volumetric defects. Int J Fatigue 2021;144:106063.
[5] Shahriari A, Ghaffari M, Khaksar L, Nasiri A, Hadadzadeh A, Amirkhiz BS, et al. Corrosion resistance of 13wt.% Cr martensitic stainless steels: Additively manufactured CX versus wrought Ni-containing AISI 420. Corros Sci 2021;184:109362.
[6] Shahriari A, Chalasani D, Amirkhiz BS, Mohammadi M. Corrosion performance of wire arc additively manufactured NAB alloy. npj Mater Degrad 2023;7(1):85.
[7] Masuo H, Tanaka Y, Morokoshi S, Yagura H, Uchida T, Yamamoto Y, et al. Influence of defects, surface roughness and HIP on the fatigue strength of Ti-6Al-4V manufactured by additive manufacturing. Int J Fatigue 2018;117:163–79.
[8] Shrestha R, Simsiriwong J, Shamsaei N. Fatigue behavior of additive manufactured 316L stainless steel parts: Effects of layer orientation and surface roughness. Addit Manuf 2019;28:23–38.
[9] Liu Z, Wang SH, Feng YJ, Wang XW, Peng YW, Gong JM. Exploration on the fatigue behavior of low-temperature carburized 316L austenitic stainless steel at elevated temperature. Mat Sci Eng a-Struct 2022;850:143562.
[10] Liu Z, Wang SH, Feng YJ, Peng YW, Gong JM, Somers MAJ. Residual stress relaxation in the carburized case of austenitic stainless steel under alternating loading. Int J Fatigue 2022;159:106837.
[11] Sander G, Tan J, Balan P, Gharbi O, Feenstra DR, Singer L, et al. Corrosion of additively manufactured alloys: a review. Corrosion 2018;74(12):1318–50.
[12] Aghayar Y, Moazzen P, Behboodi B, Shahriari A, Shakerin S, Lloyd A, et al. Laser Powder Bed Fusion of Pure Copper Electrodes. Mater Des 2024;112742.
[13] Liu Z, Zhang S, Wang SH, Peng YW, Gong JM, Somers MAJ. On the fatigue behavior of low-temperature gaseous carburized 316L austenitic stainless steel: Experimental analysis and predictive approach. Mat Sci Eng a-Struct 2020;793:139651.
[14] Hlinka J, Kraus M, Hajnys J, Pagac M, Petru J, Brytan Z, et al. Complex corrosion properties of AISI 316L steel prepared by 3D printing technology for possible implant applications. Materials (Basel) 2020;13(7):1527.
[15] Merot P, Morel F, Mayorga LG, Pessard E, Buttin P, Baffie T. Observations on the influence of process and corrosion related defects on the fatigue strength of 316L stainless steel manufactured by Laser Powder Bed Fusion (L-PBF). Int J Fatigue 2022;155:106552.
[16] Kong DC, Ni XQ, Dong CF, Zhang L, Man C, Yao JZ, et al. Heat treatment effect on the microstructure and corrosion behavior of 316L stainless steel fabricated by selective laser melting for proton exchange membrane fuel cells. Electrochim Acta 2018;276:293–303.
[17] Lodhi MJK, Deen KM, Greenlee-Wacker MC, Haider W. Additively manufactured 316L stainless steel with improved corrosion resistance and biological response for biomedical applications. Addit Manuf 2019;27:8–19.
[18] Collazo A, Figueroa R, Pérez C, Nóvoa XR. Effect of laser speed and hatch spacing on the corrosion behavior of 316L stainless steel produced by selective laser melting. Materials 2022;15(4):1353.
[19] Saeidi K, Gao X, Zhong Y, Shen ZJ. Hardened austenite steel with columnar subgrain structure formed by laser melting. Mater Sci Eng A 2015;625:221–9.
[20] Kong D, Dong C, Ni X, Li X. Corrosion of metallic materials fabricated by selective laser melting. npj Mater Degrad 2019;3(1):24.
[21] Ettefagh AH, Guo S, Raush J. Corrosion performance of additively manufactured stainless steel parts: A review. Addit Manuf 2021;37:101689.
[22] Nie J, Wei L, Jiang Y, Li Q, Luo H. Corrosion mechanism of additively manufactured 316 L stainless steel in 3.5 wt.% NaCl solution. Mater Today Commun 2021;26:101648.
[23] Melia MA, Rosenberg SG, Kotula PG, Bocher F, Schaller RF. Initial stages of oxide growth on AM stainless steel exposed to a supercritical CO2 environment. Corros Sci 2022;201:110259.
[24] Cho S, Buchsbaum SF, Biener M, Jones J, Melia MA, Stull JA, et al. True active surface area as a key indicator of corrosion behavior in additively manufactured 316l stainless steel. Mater Des 2024;237:112559.
[25] Vilaro T, Colin C, Bartout JD, Nazé L, Sennour M. Microstructural and mechanical approaches of the selective laser melting process applied to a nickel-base superalloy. Mat Sci Eng a-Struct 2012;534:446–51.

[26] Laleh M, Hughes AE, Xu W, Cizek P, Tan MYJ. Unanticipated drastic decline in pitting corrosion resistance of additively manufactured 316L stainless steel after high-temperature post-processing. Corros Sci 2020;165:108412.
[27] Chao Q, Cruz V, Thomas S, Birbilis N, Collins P, Taylor A, et al. On the enhanced corrosion resistance of a selective laser melted austenitic stainless steel. Scr Mater 2017;141:94–8.
[28] Lodhi MJK, Deen KM, Haider W. Corrosion behavior of additively manufactured 316L stainless steel in acidic media. Materialia 2018;2:111–21.
[29] Wang XY, Li DY. Mechanical and electrochemical behavior of nanocrystalline surface of 304 stainless steel. Electrochim Acta 2002;47(24):3939–47.
[30] Ganesh P, Giri R, Kaul R, Sankar PR, Tiwari P, Atulkar A, et al. Studies on pitting corrosion and sensitization in laser rapid manufactured specimens of type 316L stainless steel. Mater Des 2012;39:509–21.
[31] Trelewicz JR, Halada GP, Donaldson OK, Manogharan G. Microstructure and Corrosion Resistance of Laser Additively Manufactured 316L Stainless Steel. JOM 2016;68(3):850–9.
[32] Andreatta F, Lanzutti A, Vaglio E, Totis G, Sortino M, Fedrizzi L. Corrosion behaviour of 316L stainless steel manufactured by selective laser melting. Materials and Corrosion-Werkstoffe Und Korrosion 2019;70(9):1633–45.
[33] Kong DC, Dong CF, Ni XQ, Zhang L, Luo H, Li RX, et al. The passivity of selective laser melted 316L stainless steel. Appl Surf Sci 2020;504:144495.
[34] Hashim M, Farhad F, Smyth-Boyle D, Akid R, Zhang X, Withers PJ. Behavior of 316L stainless steel containing corrosion pits under cyclic loading. Materials and Corrosion-Werkstoffe Und Korrosion 2019;70(11):2009–19.
[35] Li SX, Akid R. Corrosion fatigue life prediction of a steel shaft material in seawater. Eng Fail Anal 2013;34:324–34.
[36] Zerbst U, Madia M, Klinger C, Bettge D, Murakami Y. Defects as a root cause of fatigue failure of metallic components. III: Cavities, dents, corrosion pits, scratches. Eng Fail Anal 2019;97:759–76.
[37] Ebara R. Corrosion fatigue crack initiation in 12% chromium stainless steel. Mater Sci Eng A 2007;468:109–13.
[38] Wu QG, Chen XD, Fan ZC, Nie DF, Wei RC. Corrosion fatigue behavior of FV520B steel in water and salt-spray environments. Eng Fail Anal 2017;79:422–30.
[39] Hu P, Meng QC, Hu WP, Shen F, Zhan ZX, Sun LL. A continuum damage mechanics approach coupled with an improved pit evolution model for the corrosion fatigue of aluminum alloy. Corros Sci 2016;113:78–90.
[40] Li YF, Farrington GC, Laird C. Cyclic response-electrochemical interaction in mono- and polycrystalline AISI 316L stainless steel in H2SO4 solution—I. The influence of mechanical strain on the transient dissolution behavior during corrosion fatigue. Acta metallurgica et materialia 1993;41(3):693–708.
[41] Kong DC, Dong CF, Ni XQ, Zhang L, Luo H, Li RX, et al. Superior resistance to hydrogen damage for selective laser melted 316L stainless steel in a proton exchange membrane fuel cell environment. Corros Sci 2020;166:108425.
[42] Balbín JA, Chaves V, Larrosa NO. Pit to crack transition and corrosion fatigue lifetime reduction estimations by means of a short crack microstructural model. Corros Sci 2021;180:109171.
[43] Gangloff RP. Corrosion fatigue crack propagation in metals, NASA Contractor Report 4301, 1990.
[44] Kim S, Burns JT, Gangloff RP. Fatigue crack formation and growth from localized corrosion in Al–Zn–Mg–Cu. Eng Fract Mech 2009;76(5):651–67.
[45] Turnbull A. Corrosion pitting and environmentally assisted small crack growth. Proc Royal Soc A: Mathematical, Phys Eng Sci 470(2169) (2014) 20140254.
[46] Turnbull A, McCartney LN, Zhou S. A model to predict the evolution of pitting corrosion and the pit-to-crack transition incorporating statistically distributed input parameters, Environment-induced cracking of materials, Elsevier; 2008, pp. 19-45.
[47] Turnbull A, McCartney LN, Zhou S. Modelling of the evolution of stress corrosion cracks from corrosion pits. Scr Mater 2006;54(4):575–8.
[48] Lou X, Othon MA, Rebak RB. Corrosion fatigue crack growth of laser additively-manufactured 316L stainless steel in high temperature water. Corros Sci 2017;127:120–30.
[49] Lou X, Song M, Emigh PW, Othon MA, Andresen PL. On the stress corrosion crack growth behaviour in high temperature water of 316L stainless steel made by laser powder bed fusion additive manufacturing. Corros Sci 2017;128:140–53.
[50] Gnanasekaran B, Song J, Vasudevan V, Fu Y. Corrosion fatigue characteristics of 316L stainless steel fabricated by laser powder bed fusion. Metals 2021;11(7):1046.
[51] Stern F, Becker L, Tenkamp J, Boes J, Lentz J, Weber S, et al. Influence of nitrogen content on the corrosion fatigue behavior of additively manufactured AISI 316L stainless steel in chloride solution. Int J Fatigue 2023;172:107666.
[52] Shaikh H, Poonguzhali A, Sivaibharasi N, Dayal RK, Khatak HS. Corrosion fatigue of aisi type 316ln stainless steel and its weld metal. Corrosion 2009;65(1):37–48.
[53] Maruyama N, Mori D, Hiromoto S, Kanazawa K, Nakamura M. Fatigue strength of 316L-type stainless steel in simulated body fluids. Corros Sci 2011;53(6):2222–7.
[54] Chen S-G, Gao H-J, Wu Q, Gao Z-H, Zhou X. Review on residual stresses in metal additive manufacturing: formation mechanisms, parameter dependencies, prediction and control approaches. J Mater Res Technol 2022;17:2950–74.
[55] Pidge PA, Kumar H. Additive manufacturing: A review on 3 D printing of metals and study of residual stress, buckling load capacity of strut members. Mater Today: Proc. 21 (2020) 1689-1694.
[56] Sander G, Babu AP, Gao X, Jiang D, Birbilis N. On the effect of build orientation and residual stress on the corrosion of 316L stainless steel prepared by selective laser melting. Corros Sci 2021;179:109149.
[57] Cruz V, Chao Q, Birbilis N, Fabijanic D, Hodgson PD, Thomas S. Electrochemical studies on the effect of residual stress on the corrosion of 316L manufactured by selective laser melting. Corros Sci 2020;164:108314.
[58] ISO 1143:2021, Metallic materials- Rotating bar bending fatigue testing; 2021.
[59] ASTM Standard Practice for Microetching Metals and Alloys; ASTM E407-07 (2015), Last Updated: Jan 21, 2016.
[60] ASTM E8/E8M-21. Standard Test Methods for Tension Testing of Metallic Materials; Last Updated Jul; 19: 2022.
[61] ISO 14577-1:2015 , Metallic materials, Instrumented indentation test for hardness and materials parameters; 2015.
[62] Zakaria KA, Abdullah S, Ghazali MJ. A review of the loading sequence effects on the fatigue life behaviour of metallic materials. J Eng Sci Technol Rev 2016;9(5).
[63] Murakami Y. Metal fatigue: effects of small defects and nonmetallic inclusions. Academic Press; 2019.
[64] Murakami Y, Endo M. Effects of defects, inclusions and inhomogeneities on fatigue strength. Int J Fatigue 1994;16(3):163–82.
[65] Rokhlin SI, Kim JY, Nagy H, Zoofan B. Effect of pitting corrosion on fatigue crack initiation and fatigue life. Eng Fract Mech 1999;62(4–5):425–44.
[66] Duan ZW, Man C, Dong CF, Cui ZY, Kong DC, Wang L, et al. Pitting behavior of SLM 316L stainless steel exposed to chloride environments with different aggressiveness: Pitting mechanism induced by gas pores. Corros Sci 2020;167:108520.
[67] Fattah-Alhosseini A, Vafaeian S. Comparison of electrochemical behavior between coarse-grained and fine-grained AISI 430 ferritic stainless steel by Mott-Schottky analysis and EIS measurements. J Alloy Compd 2015;639:301–7.
[68] Feng Z, Cheng X, Dong C, Xu L, Li X. Passivity of 316L stainless steel in borate buffer solution studied by Mott-Schottky analysis, atomic absorption spectrometry and X-ray photoelectron spectroscopy. Corros Sci 2010;52(11):3646–53.
[69] Gelderman K, Lee L, Donne SW. Flat-band potential of a semiconductor: using the Mott-Schottky equation. J Chem Educ 2007;84(4):685.
[70] Merot P, Morel F, Pessard E, Mayorga LG, Buttin P, Baffie T. Fatigue strength and life assessment of L-PBF 316L stainless steel showing process and corrosion related defects. Eng Fract Mech 2022;276:108883.
[71] Sachs NW. Understanding the surface features of fatigue fractures: how they describe the failure cause and the failure history. J Fail Anal Prev 2005;5:11–5.
[72] Hazra M, Singh AK. Failure analysis of bolt of rear mounting trunion of an aero-engine: a case of bending induced chevron pattern as well as fatigue failure on the same fracture surface. Int J Eng Mater Manuf 2021;6(1):34–42.
[73] Alam MM, Barsoum Z, Jonsén P, Häggblad H-Å. Kaplan A.Geometrical aspects of the fatigue behaviour of laser hybrid fillet welds. Cetim 2009.
[74] Padasale B, Kumar JKR, Sondar PR, Govindarajan S, Hegde SR. Failure analysis of cooling tower fan-arm. J Fail Anal Prev 2020;20:1417–25.
[75] Wang QY, Kawagoishi N, Chen Q. Effect of pitting corrosion on very high cycle fatigue behavior. Scr Mater 2003;49(7):711–6.
[76] Zuñiga Tello IF, Milković M, Domínguez Almaraz GM, Gubeljak N. Ultrasonic and conventional fatigue endurance of aeronautical aluminum alloy 7075–T6, with artificial and induced pre-corrosion. Metals 2020;10(8):1033.
[77] Almaraz GMD, Aburto AD, Gómez EC. Ultrasonic fatigue endurance of aluminum alloy AISI 6061–T6 on Pre-corroded and non-corroded specimens. Metall Mater Trans 2014;45(1):280.
[78] Khan MU, Ahmad S, Al-Gahtani HJ. Chloride-induced corrosion of steel in concrete: an overview on chloride diffusion and prediction of corrosion initiation time. Int J Corrosion 2017;2017.
[79] Milella PP. Fatigue and corrosion in metals. Springer Science & Business Media; 2012.
[80] Kalaie MR, Aghayar Y, Hadadzadeh A, Aranas C, Amirkhiz BS, Mohammadi M. Twinning-Induced plasticity behavior of pulse laser powder bed-fused 316L stainless steels. J Mater Eng Perform 2023:1–18.
[81] Nadot M. Ranganathan, Beranger, Fatigue life assessment of nodular cast iron containing casting defects. Fatigue Fract Eng Mater Struct 1999;22(4):289–300.
[82] Molina CA, Chapetti MD. Estimation of high cycle fatigue behaviour using a threshold curve concept. Int J Fatigue 2018;108:47–52.
[83] Gerberich WW, Harvey SE, Kramer DE, Hoehn JW. Low and high cycle fatigue—A continuum supported by AFM observations. Acta Mater 1998;46(14):5007–21.
[84] Riemer A, Leuders S, Thöne M, Richard HA, Tröster T, Niendorf T. On the fatigue crack growth behavior in 316L stainless steel manufactured by selective laser melting. Eng Fract Mech 2014;120:15–25.
[85] Schijve J, Campoli G, Monaco A. Fatigue of structures and secondary bending in structural elements. Int J Fatigue 2009;31(7):1111–23.
[86] Liao X, Qiang B, Wu J, Yao C, Wei X, Li Y. An improved life prediction model of corrosion fatigue for T-welded joint. Int J Fatigue 2021;152:106438.
[87] Liao X, Li Y, Qiang B, Wu J, Yao C, Wei X. An improved crack growth model of corrosion fatigue for steel in artificial seawater. Int J Fatigue 2022;160:106882.
[88] Liao X, Huang Y, Qiang B, Yao C, Wei X, Li Y. Corrosion fatigue tests in synthetic seawater with constant temperature liquid circulating system. Int J Fatigue 2020;135:105542.